Control of fossil-fuel particulate black carbon and organic matter, possibly the most effective method of slowing global warming

Mark Z. Jacobson

Department of Civil and Environmental Engineering, Stanford University, Stanford, California, USA

Received 9 October 2001; revised 5 February 2002; accepted 12 April 2002; published 15 October 2002.

[1] Under the 1997 Kyoto Protocol, no control of black carbon (BC) was considered. Here, it is found, through simulations in which 12 identifiable effects of aerosol particles on climate are treated, that any emission reduction of fossil-fuel (f.f.) particulate BC plus associated organic matter (OM) may slow global warming more than may any emission reduction of CO_2 or CH_4 for a specific period. When all f.f. BC + OM and anthropogenic CO_2 and CH_4 emissions are eliminated together, the period is 25–100 years. It is also estimated that historical net global warming can be attributed roughly to greenhouse gas plus f.f. BC + OM warming minus substantial cooling by other particles. Eliminating all f.f. BC + OM could eliminate 20–45% of net warming (8–18% of total warming before cooling is subtracted out) within 3–5 years if no other change occurred. Reducing CO_2 emissions by a third would have the same effect, but after 50–200 years. Finally, diesel cars emitting continuously under the most recent U.S. and E.U. particulate standards (0.08 g/mi; 0.05 g/km) may warm climate per distance driven over the next 100+ years more than equivalent gasoline cars. Thus, fuel and carbon tax laws that favor diesel appear to promote global warming. Toughening vehicle particulate emission standards by a factor of 8 (0.01 g/mi; 0.006 g/km) does not change this conclusion, although it shortens the period over which diesel cars warm to 13–54 years. Although control of BC + OM can slow warming, control of greenhouse gases is necessary to stop warming. Reducing BC + OM will not only slow global warming but also improve human health. *INDEX TERMS:* 0305 Atmospheric Composition and Structure: Aerosols and particles (0345, 4801); 0320 Atmospheric Composition and Structure: Cloud physics and chemistry; 0345 Atmospheric Composition and Structure: Pollution—urban and regional (0305); 1620 Global Change: Climate dynamics (3309)

Citation: Jacobson, M. Z., Control of fossil-fuel particulate black carbon and organic matter, possibly the most effective method of slowing global warming, *J. Geophys. Res.*, *107*(D19), 4410, doi:10.1029/2001JD001376, 2002.

1. Introduction

[2] To date, several studies have advocated non-CO_2 greenhouse-gas emission controls in conjunction with CO_2 emission controls as a method of slowing global warming [e.g., *Hayhoe et al.*, 1999; *Hansen et al.*, 2000; *Smith et al.*, 2000; *IPCC*, 2001]. With respect to particulates, early global radiative studies of black carbon (BC) treated it as either externally mixed or well mixed internally [e.g., *Haywood et al.*, 1997]. *Jacobson* [2000] argued that treating BC as well mixed internally was not physical and treating it as externally mixed was not representative of the real mixing state of BC. It was hypothesized that a more representative optical treatment of BC might be that of a core surrounded by shell. Under that assumption, the global direct forcing of fossil fuel plus biomass-burning BC was 0.5 W/m^2, implying that BC control might slow global warming to some degree. This implication was subsequently supported by *Hansen et al.* [2000] and *Smith et al.* [2000]. An unstudied issue, though, was the actual mixing state of BC. *Jacobson* [2001a] performed simulations of the evolution of the global scale mixing state and direct forcing of BC. It was found that both appeared to approach those of an internal mixture with a core rather than those of an external mixture, supporting the contention that BC has a strong direct forcing and its control might slow global warming.

[3] Among constituents causing warming, anthropogenic CO_2, BC, and CH_4 may have the greatest direct forcing, although other gases and particles also contribute to global warming. Other warming gases include tropospheric O_3 (whose production also leads to the formation of particulate nitrate and secondary organics, which enhance cooling), halocarbons, and N_2O. Other warming particle components include iron, aluminum, ammonium, polycyclic aromatics, and nitrated aromatics [*Jacobson*, 2001b]. To date, one study has examined the short-term climate response to size-resolved aerosols containing BC as a core on the urban scale [*Jacobson*, 1997a, 1997b], but no study has compared the effects over time of reducing BC, CO_2, and CH_4 emissions on the global scale.

[4] To estimate the relative global-scale climate benefits of BC, CO_2, and CH_4 emission controls, time-dependent

0148-0227/02/2001JD001376$09.00

global model simulations were carried out. The model used in this study is described in section 2. During the simulations, aerosol particles fed back to temperatures in at least 12 ways. These are described in section 3. Subsequent sections of this paper describe the simulations (section 4), comparisons of baseline predictions with observations (section 5), climate response results (section 6), and a comparison of the effects of diesel and gasoline on global warming (section 7).

2. Description of the Model

[5] The model used was GATOR-GCMM (Gas, Aerosol, Transport, Radiation, General Circulation, and Mesoscale Meteorological model) [*Jacobson*, 1994, 1997a, 1997b, 2001c, 2001d]. The model treated time-dependent gas, aerosol, cloud, radiative, dynamical, and transport processes over a 4°S–N × 5°W–E grid with 39 sigma-pressure layers (23 tropospheric, 16 stratospheric; 3 in the bottom 1 km) from the ground to 0.425 mb (≈55 km).

2.1. Gas Processes

[6] Gas processes included emissions, photochemistry, transport (section 2.3), homogeneous nucleation (section 2.2), condensational growth (section 2.2), dissolutional growth (section 2.2), dry deposition, and washout (section 2.5).

[7] Monthly gridded emission rates of CO_2, CO, CH_4, NO_x, SO_2, ethene, propene, ethane, and propane from biomass burning were obtained by multiplying a mean biomass-burning emission factor for each gas [*Ferek et al.*, 1998] with the monthly gridded BC biomass-burning emission inventory of *Cooke and Wilson* [1996], then dividing by a mean emission factor of BC [*Ferek et al.*, 1998]. The BC inventory for biomass burning from Cooke and Wilson was designed for the mid-1980s and gives a BC emission rate of 6 Tg C/yr. *Andreae and Merlet* [2002] calculated a BC emission rate from biomass burning of 4.7 Tg C/yr using emission factors derived therein plus estimates of biomass burned given by *Lobert et al.* [1999], which were based on data from 1980 to the early 1990s. To account for the more recent work, the gas inventory for biomass burning was reduced by 25%.

[8] Other emitted gases included volcanic SO_x [*Andres and Kasgnoc*, 1998], NO_x and other SO_x [*Voldner et al.*, 1999], NH_3 [*Bouwman et al.*, 1997], CH_4 [*Stern and Kaufman*, 1998], CO_2 [*Marland et al.*, 1999], and CO, N_2O, and NMVOCs [*Olivier et al.*, 1996]. Ocean emission rates of DMS were calculated with the parameterization of *Liss and Merlivat* [1986] and seawater DMS concentrations of *Kettle et al.* [1999]. NO_x from intercloud lightning was determined by integrating the number of bounceoffs following collisions among size-resolved ice crystals and graupel, calculating an intracloud flash rate from bounceoffs using an equation of *Wang and Prinn* [2000], assuming the cloud–ground flash rate was 35% of the cloud–cloud flash rate [*Boccippio et al.*, 2001], and assuming 1.9×10^{26} NO molecules per cloud–cloud flash and 1.9×10^{27} NO molecules per cloud–ground flash (average of high and low values for each by *Wang and Prinn* [2000]).

[9] Gas photochemistry was solved among 40 gases and 109 reactions with SMVGEAR II [*Jacobson*, 1998a]. Gas dry deposition velocities were calculated with a three-resistance approach. The surface resistance [*Wesely*, 1989; *Walmsley and Wesely*, 1996] depended on landcover type, determined at 1 km resolution from *USGS* [1999].

2.2. Aerosol and Gas–Aerosol Processes

[10] The model treated one aerosol size distribution, 0.01–110 μm diameter, with 17 moving center [*Jacobson*, 1997a] size bins in each grid cell. The number concentration of total particles and the mole concentrations of H_2O(aq), H^+, NH_4^+, Na^+, H_2SO_4(aq), HSO_4^-, SO_4^{2-}, NO_3^-, Cl^-, BC, organic matter [OM = organic carbon (OC) + functional groups], and soil-dust were prognostic variables in each bin. Particle emission sources included biomass burning, sea-spray uplift, soil uplift, and f.f. combustion.

[11] Emitted biomass-burning components included BC, OM, K^+, Na^+, Ca^{2+}, Mg^{2+}, NH_4^+, Cl^-, SO_4^{2-}, and NO_3^-. Since K^+, Ca^{2+}, and Mg^{2+} were not carried in the simulations, their mole-equivalent emissions were added to those of Na^+. Monthly gridded emission rates of each species were obtained in the same manner as were biomass-burning gases (section 2.1). Particulate emissions from biomass burning were distributed lognormally over model size bins [*Reid and Hobbs*, 1998].

[12] Emitted sea-spray and spume-drop components included H_2O, K^+, Na^+, Ca^{2+}, Mg^{2+}, Cl^-, and SO_4^{2-}. Again, since K^+, Ca^{2+}, and Mg^{2+} were not carried in the model, their mole-equivalent emissions were added to those of Na^+. Sea-spray and spume-drop emissions versus size were calculated as a function of wind speed from the works of *Monahan et al.* [1986] and *Wu* [1993], respectively. Emitted drop composition was set to that of seawater.

[13] Due to the computational burden, the only emitted soil component in the model was an unreactive, generic soil component. Soil emissions versus size were calculated from the work of *Marticorena et al.* [1997] using soil distribution data from *FAO* [1995]. The soil emission rate depended on wind speed, soil type, and particle size.

[14] Emitted f.f. particulate components included BC + OM. The f.f. BC inventory was obtained from the work of *Cooke et al.* [1999] and applied over a lognormal combustion distribution for f.f. [*Maricq*, 1999a]. Although the inventory of Cooke et al. was designed for the 1980s and may have overestimated powerplant emission factors, *Streets et al.* [2001] found that the overall current inventory of BC from China was not too different from that of Cooke et al. because Cooke et al. did not include residential combustion of biofuel emission sources of BC. Table 1 here shows that the model underpredicted BC in urban and many rural areas, suggesting that the BC inventory did not lead to overestimates of BC climate effects. Baseline OM/BC emission ratios from f.f. were set to 3.1:1 (an average OC/EC f.f. ratio from the work of *Strader et al.* [1999] is 2.4, and the OM/OC ratio was 1.3:1). The OM/BC emission ratio for biomass burning was 8:1.

[15] H_2SO_4–H_2O homogenous nucleation was calculated with classical theory [*Hamill et al.*, 1982; *Zhao and Turco*, 1995] and solved simultaneously with condensation of H_2SO_4–H_2O between the gas phase and all 17 bins with a mass-conserving, noniterative, and unconditionally stable condensation scheme [*Jacobson*, 1997c]. In addition, dissolution of each NH_3, HNO_3, and HCl was solved between

Table 1. Comparison of Modeled Versus Observed Near-Surface BC Concentrations

Station	Latitude	Longitude	Modeled BC (ng/m^3)	Measured BC (ng/m^3)	Period	Data reference
				Marine		
Amsterdam Island	37°30′S	77°10′E	8.5	5.5	Annual	*Cachier et al.* [1994]
Atlantic Ocean	31–37°N	66–76°W	160	10	January–February	*Quinn et al.* [2001]
	15–31°N	43–66°W	45	10		
	8–15°N	33–43°W	65	30		
	3–8°N	26–33°W	220	360		
	5°S–3°N	17–26°W	180	380 ± 210		
	25–5°S	6°E–17°W	50	20 ± 30		
	33–24°S	18–6°E	90	10		
Bermuda	32°45′N	65°W	70	30	February	*Wolff et al.* [1986]
			80	40	August	
Bõisto Island	60°20′N	26°30′E	1030	50–1000	June	*Raunemaa et al.* [1993]
Chichi-jima	27°N	142°E	175	610	December	*Ohta and Okita* [1984]
Corsica	42°N	9°E	420	380	Spring	*Cachier et al.* [1989]
East China Sea	27–32°N	127–129°E	370	355	April–May	*Parungo et al.* [1994]
	27–33°N	124–129°E	810	505	October–November	
	28–32°N	125–128°E	920	133	December	
Hachi-jima	33°5′N	139°45′E	885	1070	January	*Ohta and Okita* [1984]
			845	740	December	
Halley Bay	75°24′S	27°W	2.7	0.3–3		*Cachier et al.* [1986], *Hansen et al.* [1988]
La Réunion Island	21°30′S	55°30′E	70	50–650	Annual	*Bhugwant et al.* [2000]
Mace Head, Ireland	53°20′N	9°54′W	490	26 (17–34)	July–August	*Krivacsy et al.* [2001]
			450	47–1041	Annual	*Derwent et al.* [2001]
NE Atlantic			80	268	October–November	*O'Dowd et al.* [1993]
NE Pacific	27–48°N	175°E	60	150–300	April–October	*Kaneyasu and Murayami* [2000]
Ny-Alesund	78°54′N	11°53′E	150	70 (28–174)	March–May	*Heintzenberg* [1982]
			170	293 (123–567)	March–April	*Clarke* [1989]
Oki Island	36°9′N	133°12′W	55	520	Annual	*Mukai et al.* [1990]
San Nicolas Island	33°9′N	119°18′W	240	260	Annual	*Kim et al.* [2000]
				Rural		
Abastumani	41°30′N	42°40′E	460	980	Annual	*Dzubay et al.* [1984]
Abisko	68°18′N	18°30′E	300	393	March–April	*Noone and Clarke* [1988]
			360	259–780	Annual	*Clarke* [1989]
Allegheny	40°N	79°W	820	1300	August	*Keeler et al.* [1990]
Aspvreten, Sweden	58°48′N	17°23′W	115	100 (50–170)	June–July	*Zappoli et al.* [1999]
Cheboque Point	43°48′N	66°6′W	270	81–139	August–September	*Chylek et al.* [1996]
East Arctic	79°33′N	90°37′E	125	25–115	March–April	*Polissar* [1993]
Ecuador	2°S	77.18°W	265	100–520	Annual	*Andreae et al.* [1984]
	2°15′S	79°52′W	430	100–520	June	
Florida	28°N	82°W	690	400	Annual	*Andreae et al.* [1984]
Gif sur Yvette	48°42′N	2°8′E	1300	1650–2750	Seasonal	*Cachier et al.* [1989]; *Brémond et al.* [1989]
Jungfraujoch, Switzerland	46°33′N	7°59′E	710	290 (8–720)	July–August	*Krivacsy et al.* [2001]
K-Puszta, Hungary	46°57′N	19°42′E	1670	810	Annual	*Heintzenberg and Mészáros* [1985]
			1700	600 (400–600)	July–August	*Zappoli et al.* [1999]
			1700	750 (120–1890)	July–August	*Krivacsy et al.* [2001]
Landes forest	44°N	1°W	350	300	Autumn	*Cachier et al.* [1989]
Lin'an	30°15′N	119°42′E	2150	2070	July–August	*Parungo et al.* [1994]
North Carolina	35°18′N	80°W	550	520	Annual	*Andreae et al.* [1984]
Nylsvley, South Africa	24°39′N	28°24′E	340	850 (450–1340)	May	*Puxbaum et al.* [2000]
Petten	52°54′N	2°55′E	1360	1630	April	*Berner et al.* [1996]
Rorvik	57°18′N	12°12′E	1010	725	January–May	*Broström-Lundén et al.* [1994]
Senonche	48°34′N	12°E	1100	1200	March	*Cachier et al.* [1990]
Southwest United States	34°18′N	106°W	160	150–220	Annual	*Andreae et al.* [1984]
West Mountain	40°N	116°E	720	1710–2610	August	*Parungo et al.* [1994]
Maldives	4°58′N	73°28′E	290	2700–9400	February	*Chowdhury et al.* [2001]
				Urban		
Arnhem	52°N	5°54′E	1600	2950	October–November	*Janssen et al.* [1997]
Atlanta, Ga.	33°N	85°W	460	1500 (500–3000)	August	*Modey et al.* [2001]
Baltimore			800	530–2600	July	*Brunciak et al.* [2001]
Beijing	40°N	116°E	680	8700–10,100	Annual	*He et al.* [2001]
			700	6270	Summer	
			640	10,230	Autumn	
			690	11,080	Winter	
			680	6670	Spring	
Chicago/Lake Michigan	41°31′N	87°39′W	970	340–420	January	*Offenberg and Baker* [2000]
			1050	350–490	July	
Chesapeake Bay	38°40′N	76°25′W	790	400–7300	July	*Brunciak et al.* [2001]
Clermont Ferrand	45°46′N	34°E	1270	2400	April	*Lyubovtseva and Yatskovich* [1989]

Table 1. (continued)

Station	Latitude	Longitude	Modeled BC (ng/m^3)	Measured BC (ng/m^3)	Period	Data reference
Dushanbe	38°33′N	68°48′E	290	10,700–12,000	August–September	*Hansen et al.* [1993]
Gorlitz	51°10′N	14°59′E	1950	1300	Annual	*Zier* [1991]
Halle	51°29′N	12°E	1800	1600	Annual	*Zier* [1991]
Hamburg	53°52′N	9°59′E	2800	1975	Annual	*Heintzenberg and Mészáros* [1985]
Kaohsiung			1400	3300–8000	November–April	*Lin and Tai* [2001]
Kap Arkona	57°37′N	13°21′E	810	400	Annual	*Zier* [1991]
Leeds	53°48′N	1°34′W	1020	780–1300	Summer, Winter	*Willison et al.* [1985]
Los Angeles Basin	34°4′N	118°15′W	390	2750–4230	Annual	*Kim et al.* [2000]
Moscow	55°45′N	37°35′E	1260	3500–6750	Summer, Winter	*Kopeykin et al.* [1993]
Mount Gibbes	35°78′N	82°29′E	240	74	Winter	*Im et al.* [2001]
			200	230	Summer	
Nagoya	35°10′N	136°50′E	800	13,000	Annual	*Kadowaki* [1990]
Orleans	47°54′N	15°2′E	1180	2900	March	*Del Delumyea and Kalivretenos* [1987]
Paris	48°50′N	2°20′E	1340	4600	Annual	*Ruellan and Cachier* [2001]
			1600	13,600	Summer–Autumn	
Potsdam	52°3′N	13°4′E	1950	1000	Annual	*Zier* [1991]
Po Valley, Italy	44°39′N	11°37′E	800	1000 (500–1500)	September	*Zappoli et al.* [1999]
Radebeul	51°6′N	13°55′E	2200	1400	Annual	*Zier* [1991]
Santiago	33°33′S	70°36′W	90	30,600	June	*Didyk et al.* [2000]
Seoul	37°20′N	126°35′E	2340	8400	June	*Park et al.* [2001]
Thessaloniki	40°31′N	22°58′E	1080	3500–8900	June	*Chazette and Liousse* [2001]
Uji	34°32′N	135°29′E	860	5210	Winter	*Hitzenberger and Tohno* [2001]
			680	2600	Summer	
			770	4890	Annual	
Vienna	48°12′N	16°22′E	1370	6580	Winter	*Hitzenberger and Tohno* [2001]
			1890	2600	Summer	
			1550	4890	Annual	

the gas phase and 17 particle size bins with an analogous dissolution scheme [*Jacobson*, 1997c]. SO_2 dissolution and aqueous chemistry in aerosol particles and cloud drops were treated as described in section 2.5.

[16] Aerosol liquid water content, pH, and ion distributions in all size bins were solved with EQUISOLV II [*Jacobson*, 1999b]. Aerosol–aerosol coagulation (assuming kernels for Brownian motion, Brownian diffusion enhancement, gravitational collection, turbulent inertial motion, and turbulent shear) was solved among all components and total particles in each bin with a volume-conserving, noniterative, scheme [*Jacobson et al.*, 1994]. Aerosol–cloud coagulation, aerosol rainout, and aerosol washout are discussed in section 2.5. Particle sedimentation and dry deposition were solved as described by *Jacobson* [1999a, Chapter 20].

2.3. Dynamics and Transport

[17] The global dynamics module integrates equations for momentum (under the hydrostatic assumption), thermodynamic energy, and total water. The solution is a fourth-order scheme that conserves potential enstrophy and energy [*Arakawa and Lamb*, 1981]. Transport of gases and aerosols was carried out with the scheme of *Walcek and Aleksic* [1998] using online winds predicted by the dynamics module and vertical diffusion coefficients predicted by the turbulence module.

2.4. Turbulence, Stratus Clouds, Cumulus Clouds, and Species Transport in Clouds

[18] The turbulence closure (order 2.5) and stratus cloud parameterizations in the model were coupled together, and both were drawn from the work of *Mellor and Yamada* [1982]. Turbulence parameters affected momentum, energy, and tracers. The stratus cloud scheme predicted stratus cloud fraction and water content in each layer given turbulence terms and vertical gradients of energy and moisture. Cloud water and fraction fed back to turbulence. Cloud water was partitioned into liquid and ice with a temperature-dependent scaling factor.

[19] Cumulus clouds were predicted with a modified Arakawa–Schubert algorithm [*Ding and Randall*, 1998]. In each grid cell, nearly 500 subgrid cumulus clouds could form, each defined by a unique cloud base and top (with up to 23 tropospheric layers, 22 bases and 22 tops were possible). The model accounted for downdrafts and predicted cumulus precipitation, liquid water content, ice content, cumulus cloud fraction, and adjustments to large-scale potential temperature, momentum, and water vapor for each subgrid cloud. The product of each subgrid cloud parameter and subgrid cloud fraction was summed over all subgrid clouds to give bulk values of the parameter for each grid cell.

[20] A free-convective plume model [*Lu and Turco*, 1994] was applied to each subgrid cumulus cloud to convect gases and aerosols between each subgrid cumulus subcloud layer and cloud top. The resulting vertical gas and aerosol distribution in each subgrid cloud was multiplied by the respective fraction of the subgrid cloud to obtain a weighted-average cloudy-sky vertical gas and aerosol distribution in each grid cell. Cloudy-sky distributions were affected by gas–aerosol–cloud interactions, as described next.

2.5. Gas–Aerosol–Cloud Interactions

[21] Size-resolved cloud liquid, ice, graupel, and precipitation in the model interacted with gases and size-resolved aerosol particles, as described here.

[22] First, summed cloud liquid, ice, and precipitation in each grid cell from the cumulus and stratus schemes, were evaporated/sublimated back to the gas phase so that the vapor could be regrown onto size-resolved ice nuclei (IN) and cloud condensation nuclei (CCN).

[23] Second, all in-cloud aerosol particle number and component mole concentrations, determined from the convective plume calculation for cumulus clouds and from the cloudy-sky fraction of the grid cell for stratus clouds, were rebinned from the 17-bin aerosol distribution to a 30-bin hydrometeor distribution. A fraction of the particles in each bin were assumed to serve as potential ice nuclei. The fraction was calculated by specifying a probability that a given component in a particle of a given size could serve as an ice nucleus, then weighting the probability by the mole fraction of the component in the bin. The probabilities were estimated from the work of *Pruppacher and Klett* [1997] who suggest that the fraction can be as low as one in a million. They suggest that nonhygroscopic supermicron particles, soil components, a small fraction of OM, certain viruses and bacteria, and a small fraction of sea salt make the best ice nuclei. Soot is not a good ice nucleus, except below -15°C and at high supersaturations. Some pollutants deactivate ice nuclei.

[24] Third, depositional growth of water vapor to ice was solved simultaneously among the portion of water vapor sublimated from cloud and precipitation total ice and the IN in each of the 30 hydrometeor size bins with a mass-conserving, noniterative and unconditionally stable scheme [*Jacobson*, 1997c]. Whether an IN activated depended on whether it exceeded the critical radius for cloud–ice growth, a prognostic parameter.

[25] Fourth, growth of water vapor to liquid was solved among the portion of water vapor evaporated from cloud and precipitation total liquid and the CCN in each size bin with the same scheme used for ice growth. The number concentration of CCN in each bin was determined as the total number concentration of aerosol particles minus the number concentration of activated IN. Whether a CCN activated depended on whether its radius exceeded the critical radius for cloud–liquid growth, a prognostic parameter.

[26] As a result of Steps 1–4, liquid water and ice size distributions were created. Each bin in each distribution contained all the aerosol particle components of the activated CCN or ice nuclei it grew upon. Thus, of the original aerosol particles and their components in each size bin, some were now incorporated within ice crystals, others were incorporated in liquid drops, and the rest were interstitial aerosol particles.

[27] Fifth, the size-resolved liquid drops and ice crystals were self-coagulated (liquid plus liquid or ice plus ice) to form larger liquid or ice particles and heterocoagulated (liquid plus ice) to form graupel with the scheme described by *Jacobson et al.* [1994] to simulate collision/coalescence. During hydrometeor self-coagulation and heterocoagulation, aerosol particle components incorporated within liquid and ice hydrometeors also coagulated to larger sizes or to the graupel distribution.

[28] Sixth, the irreversible reactions, $SO_2(g) + H_2O_2(g) \rightarrow S(VI)(aq)$ and $SO_2(g) + O_3(g) \rightarrow S(VI)(aq)$ were solved together with gas photochemistry to simulate dissolution and formation of S(VI)(aq) in liquid cloud drops and aerosol particles containing liquid water. The rates of these reactions were determined by combining their aqueous rates of reactions with the effective Henry's constant for each species and with the total cloud plus aerosol liquid water content (determined by summing liquid water over all hydrometeor and aerosol size bins). The bulk S(VI)(aq) produced was then distributed over each cloud and aerosol size bin proportionately to the liquid water volume of the bin. The incremental S(VI)(aq) assigned to each bin was added to the S(VI)(aq) already in the bin.

[29] Seventh, if precipitation occurred from a layer, the largest particles of each hydrometeor type were placed in a separate size distribution and removed from the layer as precipitation along with their associated aerosol particle components, simulating aerosol particle rainout. For each layer, the total mass of liquid water, ice, and graupel precipitated plus the sum of the remaining cloud liquid, ice, and graupel minus the mass of aerosol particles in these distributions exactly equaled the initial mass of bulk cloud plus precipitation liquid and ice from the cumulus and stratus parameterizations.

[30] Eighth, size-resolved interstitial aerosol particles and their components were heterocoagulated (again conserving volume) with each of the three size-resolved cloud hydrometeor distributions in each layer and with each of the three size-resolved precipitation hydrometeor distributions passing through each layer. The latter allowed treatment of aerosol particle washout (rainout was treated in Step 7). The precipitation passing through each layer was the sum of precipitation from all cloud layers above.

[31] Ninth, the precipitation passing through each layer was summed over all hydrometeor sizes to obtain the bulk precipitation passing through the layer. Equilibrium equations between each gas in the model and the bulk rainwater (assuming an effective Henry's constant for each gas) were solved to estimate the mole fraction of the gas from each cell partitioned into rainwater, simulating gas washout. If rainwater passing through a cell was already saturated with the gas, no additional gas could enter the rainwater.

[32] Finally, at the end of each time step the nonprecipitated cloud liquid, ice, and graupel distributions were evaporated, releasing the aerosol particle cores. The evaporated aerosol particle distribution differed from the original in-cloud distribution due to in-cloud aerosol particle growth, coagulation, chemistry, evaporation, and removal. The evaporated distributions were then weighed by cloud fraction and added to clear-sky distributions, weighted by clear-sky fraction. The liquid water content of the resulting aerosol particles was determined from an equilibrium calculation (section 2.2).

2.6. Radiative Transfer

[33] Radiative transfer was solved to determine heating rates (for temperature calculations) and actinic fluxes. Irradiances for heating rates were determined for 409 wave intervals (86, 67, and 256 in the regions <0.8, 0.8–4.5, and 4.5–1000 μm, respectively). Actinic fluxes were determined for 86 intervals <0.8 μm. Both were solved with the technique of *Toon et al.* [1989], which has an error <10% under typical scattering and absorbing conditions. In each column of the model, two calculations were performed: one with clouds, aerosols, and gases and the other

with aerosols and gases, but no clouds. Heating rates and actinic fluxes from the two calculations were then weighted by cloudy-sky and clear-sky fractions. Optical properties used for radiative transfer are described as follows.

[34] The model accounted for Rayleigh scattering and gas absorption. UV and/or visible light gas absorbers included O_2, O_3, CO_2, H_2O, NO_2, NO_3, N_2O, N_2O_5, HONO, HNO_3, HO_2NO_2, H_2O_2, HCHO, CH_3CHO, and CH_3OOH. Solar-IR absorbers included H_2O, CO_2, O_3, and O_2. Thermal-IR absorbers included H_2O, CO_2, O_3, CH_4, and N_2O. Thermal-IR absorption coefficients were from the work of *Mlawer et al.* [1997].

[35] Aerosol particle optical properties were calculated assuming that BC (if present) comprised a particle's core and all other material coated the core. BC density was 1.5 g/cm^3, and its refractive indices were taken from the work of *Krekov* [1993]. The ratio of BC's midvisible imaginary refractive index to its density was less than that of crystalline graphite, suggesting that results here may underpredict BC radiative effects. Shell refractive indices were obtained by calculating a solution and nonsolution refractive index and volume averaging the two. Solution real refractive indices were calculated from partial-molar refraction theory [e.g., *Stelson*, 1990; *Tang*, 1997]. Solution imaginary refractive indices were calculated analogously. Refractive indices for OM (a nonsolution component) were obtained from the work of *Krekov* [1993], except that UV refractive indices were weighted to account for selective UV absorption by nitrated aromatic, polycyclic aromatic, and other UV-absorbing organic compounds, as described by *Jacobson* [2001b]. Core and shell refractive indices were used in a core-shell Mie theory calculation [*Toon and Ackerman*, 1981] to determine optical properties for each particle composition and size and for each wavelength.

[36] Cloud liquid, ice, and graupel optical properties for each hydrometeor size and radiation wavelength were also determined from Mie calculations.

2.7. Subgrid Temperatures and Fluxes and Ocean Treatment

[37] The model treated ground temperatures over heterogeneous surfaces. Each grid cell was divided into up to 15 surface classes (12 soil classes and roads, roofs, and water). The model also treated vegetation over soil, snow over bare soil, snow over vegetation over soil, sea ice over water, and snow over sea ice over water. For surfaces except sea ice and water, temperatures and liquid water were found with a time-dependent 10-layer subsurface module. For sea ice, a time-dependent slab calculation was performed. For ocean water, a 2-D potential-enstrophy conserving shallow-water equation mixed-layer module, forced by wind stress (G. Ketefian, Ph.D. thesis, Stanford University, 2002, in preparation, based on the shallow-water scheme of *Arakawa and Lamb* [1981]) was used to predict ocean velocities and transport energy horizontally. The average mixing depth was 60 m although the actual depth at each location was a prognostic variable. For lake water, a fixed 60 m mixing depth was assumed. Water temperatures were also affected by sensible, latent, and radiative fluxes between water and air.

[38] At the end of a subsurface-module time step (12 s), surface temperatures, sensible heat fluxes, latent heat fluxes, water vapor fluxes, friction velocities, surface albedos, emissivities, and other parameters were weighted by the fractional surface type in the cell to give an effective parameter value for the cell as a whole. The model treatment of surfaces is discussed in detail by *Jacobson* [2001c], except that global soil moisture was initialized here with monthly gridded values from the work of *Nijssen et al.* [2001] and the global fractional vegetation cover was obtained here from the work of *Zeng et al.* [2000]. The surface albedos for snow and sea ice used here were wavelength dependent [*Grenfell et al.*, 1994; *Allison et al.*, 1993] and a function of snow and/or sea ice thickness.

3. Effects of Particles on Climate

[39] The model treated 12 identifiable effects of aerosol particles on climate. Two of these effects (the ''indirect effect'' and the ''semidirect effect'') have previously been specified in the literature. Two additional effects (the ''particle effect through surface albedo'' and the ''particle effect through large-scale meteorology'') have obvious counterparts with respect to greenhouse gases and have been accounted for in numerous previous studies. The remaining eight effects have either not been described or described only partially in the literature. Some have been accounted for in simulations.

3.1. The "Self-Feedback Effect"

[40] When new particles are emitted, they affect air temperature, relative humidity, and surface area available for gases to condense upon, all of which affect the composition, liquid water content, size, and optical properties of both the new and existing particles. This effect is referred to as the ''self-feedback effect.'' For example, when BC warms the air, it decreases the relative humidity, decreasing the liquid water content and reflectivity of particles containing sulfate and nitrate, warming the air further. At the same time, when BC is emitted in one location, it provides additional surface area for sulfuric acid to condense upon, increasing the formation of sulfate upwind and decreasing it downwind. An increase in sulfate increases its liquid water content as well. Changes in aerosol particle liquid-water also change the aqueous oxidation rate of SO_2 to sulfate and the dissolution rate of NH_3, HNO_3, and HCl into particles, further changing particle size and reflectivity. Treatment of the ''self-feedback effect'', which requires the treatment of nucleation, electrolyte hydration, dissolutional growth, condensational growth, aqueous chemistry, and the effect of aerosol particles on temperatures and the relative humidity through the thermodynamic energy equation has been accounted for in model simulations [*Jacobson*, 1994, 1997a, 1998a].

3.2. The "Photochemistry Effect"

[41] Aerosol particles alter photolysis coefficients of gases, affecting their concentrations and those of other gases (through kinetic chemistry) [e.g., *Jacobson*, 1994, 1997b, 1998b; *Dickerson et al.*, 1997]. A change in gas abundance changes solar and thermal-IR heating rates in a process called the ''photochemistry effect''. The effect of aerosols on heating rates through their modification of photolysis has been accounted for in 3-D simulations [*Jacobson*, 1994, 1997b, 1998b]. To account for the ''photochemistry effect'', changes in size-resolved particles were

allowed to affect photolysis and solar plus thermal-IR heating rates of all UV- and solar-absorbing gases and the heating rates of their by-products.

3.3. The "Smudge-Pot Effect"

[42] During day and night all aerosol particles trap the Earth's thermal-IR radiation, warming the air [*Bergstrom and Viskanta*, 1973; *Zdundowski et al.*, 1976]. This warming is well known to citrus growers who, at night, used to burn crude oil in smudge pots to fill the air with smoke and trap thermal-IR radiation, preventing crops from freezing. The warming of air relative to a surface below increases the stability of air, reducing vertical fluxes of horizontal momentum, slowing surface winds (and increasing them aloft), reducing the wind speed-dependent emission rates of sea-spray, soil-dust, road-dust, pollens, spores and some gas-phase particle precursors. The reduction in these particles affects daytime solar and daytime/nighttime thermal-IR radiation transfer. Changes in stability and winds also affect energy and pollutant transport. The effect of thermal-IR absorption by particles on the emission of other particles and gases and on local energy and pollutant transport is referred to as the ''smudge-pot effect''. In the model, aerosol particle scattering and absorption affect solar and thermal-IR heating rates, which change temperatures and stability, which feed back to winds, emissions of wind-driven aerosol particles and precursor gases, and pollutant/energy transport, allowing for the treatment of this effect.

3.4. The "Daytime Stability Effect"

[43] If airborne particles absorb solar radiation, the air warms. Whether the particles absorb or only scatter, they prevent solar radiation from reaching the surface, cooling the surface and increasing the air's stability [*Bergstrom and Viskanta*, 1973; *Venkatram and Viskanta*, 1977; *Ackerman*, 1977]. Like with the ''smudge-pot effect'', enhanced daytime stability slows surface winds, reducing emissions of wind-driven particles and gases and affecting local pollutant and energy transport. At the same time, heating at the top of the boundary layer due to aerosol absorption destabilizes the air above the boundary layer [e.g., *Jacobson*, 1998b, Figure 8]. This destabilization has little effect on emissions, since the air below is more stable, but slightly increases venting of particles at the top of the boundary layer to the free troposphere. The effect of solar absorption and scattering by particles on emissions of other particles and gases and on local energy and pollutant transport is referred to as the ''daytime stability effect''. The same processes in the model that allow treatment of the ''smudge-pot effect'' allow treatment of this effect.

3.5. "Indirect Effects"

[44] An increase in the number of particles increases the number and decreases the size of cloud drops (''first indirect effect'') [*Twomey*, 1977], reducing rates of drizzle, thereby increasing liquid water content and fractional cloudiness of low-level clouds (''second indirect effect'') [*Albrecht*, 1989]. These ''indirect effects'' increase scattering and decrease the transmission of radiation to the Earth's surface. In the model, clouds formed on top of current aerosol particle size distributions. Size-resolved cloud drops and ice crystals grew by condensation, deposition, and coagulation, and the largest resulting drops, crystals, and graupel were removed by precipitation, allowing for substantial treatment of the ''indirect effects.''

3.6. The "The Effect on BC Absorption of the First Indirect Effect"

[45] When the ''first indirect effect'' occurs, cloud scattering is enhanced, increasing the absorption of all solar radiation by BC and solar-IR radiation by water vapor and CO_2 within and above the cloud, warming the air there. Previous studies have shown that clouds enhance the direct forcing of soot lying within and above them [e.g., *Haywood et al.*, 1997; *Jacobson*, 2001b], but studies to date have not linked changes in cloud scattering due to the first indirect effect to enhanced absorption by BC or greenhouse gases.

3.7. The "Semidirect Effect"

[46] Solar absorption by a low cloud increases stability below the cloud, reducing vertical mixing of moisture to the cloud base, thinning the cloud [*Nicholls*, 1984]. Decreases in relative humidity correlate with decreases in low-cloud cover [*Bretherton et al.*, 1995; *Klein*, 1997]. Similarly, absorbing particles warm the air, decreasing its relative humidity and increasing its stability, reducing low-cloud cover [*Hansen et al.*, 1997; *Ackerman et al.*, 2000] Reduced cloud cover increases sunlight reaching the surface, warming the surface in a process called the ''semidirect effect'' [*Hansen et al.*, 1997]. In the model, in-cloud BC absorption of solar radiation allowed for this effect.

3.8. The "BC-Low-Cloud Positive Feedback Loop"

[47] When BC reduces low-cloud cover by increasing stability and decreasing relative humidity, enhanced sunlight through the air is absorbed by BC (and by water vapor and CO_2 in the solar-IR), further heating the air and reducing cloud cover in a positive feedback loop, identified here as the ''BC-low-cloud positive feedback loop''. Whereas CO_2 also warms the air by absorbing thermal-IR and solar-IR radiation, reducing low cloud cover and enhancing surface solar radiation in some cases, it absorbs less sunlight than BC, so CO_2 partake less in this feedback loop. The model allowed treatment of this effect, since solar absorption by BC, CO_2, and H_2O was affected by cloud optics.

3.9. The "Rainout Effect"

[48] When BC increases stability of and vertical moisture transport in the boundary layer, it may decrease cumulus convection, much of which starts in the boundary layer, reducing cumulus precipitation. The addition of BC also triggers the second ''indirect effect,'' which reduces precipitation. Reducing precipitation reduces rainout of soluble gases and all aerosol particles, increasing their concentrations in the air, increasing warming in some cases and cooling in others.

3.10. The "BC-Water Vapor Positive Feedback"

[49] When BC is present, it warms the air relative to the surface. The warmer air decreases the relative humidity, evaporating cloud water to vapor, a greenhouse gas, warming the air further. The resulting vertical temperature gradient, in the presence of mechanical or thermal turbulence, increases the downward sensible heat flux, warming the surface (although less than the air is warmed). The increase

in surface temperature relative to its initial temperature increases the evaporation rate of ocean and soil water. Since the air is now warmer, the saturation vapor pressure of water is now higher, allowing much of the additional water vapor to accumulate. The additional water vapor absorbs solar-IR and thermal-IR, warming the air further. (This feedback also applies to CO_2 for the most part).

3.11. The "Particle Effect Through Surface Albedo"

[50] During the day, airborne BC reduces sunlight to the ground, cooling it, increasing the lifetime of existing snow. Conversely, because BC warms the air, snow falling through the warmer air is more likely to melt. At night, airborne BC also enhances downward thermal-IR, increasing nighttime melting and sublimation of snow on the ground. Because the albedo of new snow exceeds that of sea ice, which exceeds those of soil or water, the melting of snow or sea ice increases sunlight to the surface. The effect of aerosol particles on temperatures through their change in snow and sea ice cover is referred as the "particle effect through surface albedo", analogous to its well-known greenhouse gas counterpart, the "snow-albedo effect". Any model that treats the climate response of aerosols treats this effect to some degree. A related effect is the effect of soot deposition to snow and sea ice on their albedos [e.g., *Warren*, 1984; *Vogelmann et al.*, 1988; *Warren and Clarke*, 1990; *Grenfell et al.*, 1994; *Light et al.*, 1998; *Hansen and Sato*, 2001]. This effect was not treated here. It may be more important where pollutant concentrations are high [e.g., *Light et al.*, 1998] than over the Antarctic [e.g., *Warren and Clarke*, 1990; *Grenfell et al.*, 1994].

3.12. The "Particle Effect Through Large-Scale Meteorology"

[51] Aerosol particles affect local temperatures, which affect local air pressures, winds, relative humidities, and clouds. Changes in local meteorology slightly shift the locations and magnitudes of semipermanent and thermal pressure systems and jet streams. The effect of local particles on large-scale temperatures is referred to as the "particle effect through large-scale meteorology" and has a well-known counterpart with respect to greenhouse gases. Any model that treats the climate response of aerosols treats this effect.

3.13. Difficulty in Isolating the Importance of the Effects

[52] Whereas, it would be ideal to quantify the importance of each effect described, this is not possible nor has it been done for any effect to date. Quantifying any effect of aerosol particles requires shutting off one or more physical or chemical processes; yet, each chemical and physical aerosol processes affects several effects simultaneously, not just one, so it is possible only to quantify correctly the net effect of all feedbacks on climate simultaneously, but not an individual feedback.

[53] For example, previous studies have tried to quantify the "indirect effects". In the case of the "first indirect effect" they have calculated the difference in forcing from two simulations, one with present-day CCN and another with preindustrial CCN [e.g., *IPCC*, 2001]. Such a comparison does not (nor can any comparison) correctly quantify the "first indirect effect", since in the real atmosphere, changing the number of CCN immediately triggers the "photochemistry effect", the "effect on absorption of the first indirect effect", the "smudge-pot effect", the "daytime stability effect", the "semidirect effect", the "BC-low-cloud positive feedback loop", etc., all of which feed back to temperatures and to the number of CCN. In all cases, either these models did not account for some or all of these effects, in which case their climate responses and estimated forcings were incorrect, or they really quantified the sum of multiple effects. More specifically, if a study wants to isolate the "indirect effects" due to BC correctly, it must account for all effects that affect BC (and all other aerosol) concentrations and coatings, since these parameters affect the "indirect effects" themselves. Yet, a study that includes these other effects cannot separate out their climate responses from those of the "indirect effects". Although they cannot be correctly quantified, effects can be used to explain some characteristics of climate response, as described in section 6.

4. Simulations

[54] Three sets of simulations were run: with and without (1) current levels of anthropogenic CO_2, (2) current levels of anthropogenic CH_4, and (3) emitted f.f. BC + OM. f.f. BC represents about half of global anthropogenic BC. The other half is from biomass burning. Biomass-burning emissions were included here, but this paper examines the climate response of reducing only f.f. BC + OM emissions, not biomass-burning emissions.

[55] The with/without anthropogenic CO_2 and CH_4 simulations were "equilibrium climate sensitivity" simulations [*IPCC*, 2001] comparing current and preindustrial CO_2 and CH_4 loadings, respectively. The equilibrium simulations were each run for 6 years, more than the estimated equilibrium response time of temperature to a step change in forcing in a model with a mixed-layer ocean (section 2.7) [e.g., *Hoffert et al.*, 1980]. A comparison of results from the equilibrium CO_2 simulations with radiosonde measurements and another model study is discussed in section 6. In addition, a 6 year CO_2 doubling equilibrium sensitivity was also run, and it caused a warming of 3.2 K, comparable with *IPCC* [2001] CO_2 doubling sensitivities of 1.5–4.5 K.

[56] The historic CO_2 and CH_4 equilibrium simulations were run to estimate the effect of eliminating all anthropogenic emissions of CO_2 and CH_4. Even if all anthropogenic CO_2 emissions were eliminated today, full climate response would not occur for 1000 years, since the *e*-folding lifetime of CO_2 is 50–200 years [*IPCC*, 2001], and several lifetimes are required for a perturbation to be cleared out of the atmosphere. Figure 1 scales the equilibrium results with lifetime to show how eliminating CO_2 or CH_4 emissions today might effect global near-surface temperatures over the next 100 years. The use of a mixed-layer ocean model (section 2.7) assumes that the deep ocean has little effect on temperatures over the 100 year period. Although this is a simplifying assumption, Figure 9.1 of *IPCC* [2001] suggests that the deep ocean may have little net effect on atmospheric temperatures due to perturbations to CO_2 over 80 years, and between years 80 and 100, the deep ocean dampens temperature changes due to CO_2 by about 7%. Such a dampening would appear to shift all curves in

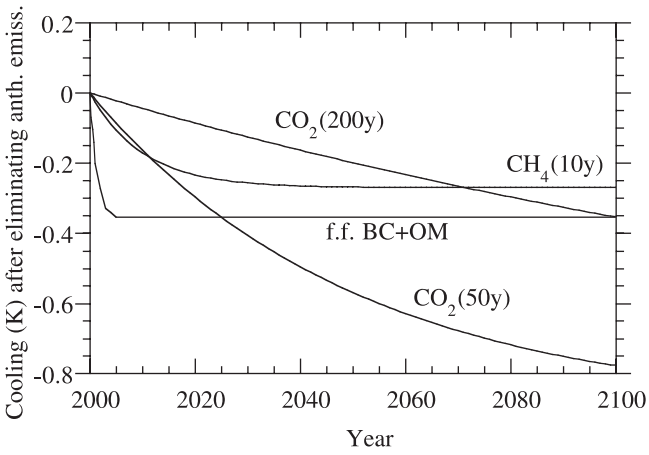

Figure 1. Estimated changes in temperature due to eliminating all anthropogenic emissions of each CO_2, CH_4, and f.f. BC + OM during the next 100 years. The curve for CO_2 and CH_4 were obtained by first running "equilibrium climate sensitivity" simulations with and without current levels of anthropogenic mixing ratios of each component for 6 years. The differences in temperatures between the with and the without cases (-0.9 K for CO_2, -0.27 K for CH_4) represent the cooling that results after eliminating the component from the atmosphere, which would occur only after many *e*-folding lifetimes of the component. The differences in temperatures were exponentially decayed from the initial time, assuming initial *e*-folding lifetimes of 50 and 200 years for CO_2 [curves CO_2 (50 years) and CO_2 (200 years), respectively] and 10 years for CH_4 [curve CH_4 (10 years)]. In the case of f.f. BC + OM, simulations were run with/without f.f. BC + OM emissions (5.1 Tg/yr BC + 10.1 Tg/yr OM) for 5 years. The curve after 5 years was held constant.

Figure 1 up proportionately after 80 years, thereby strengthening the conclusions here, since the largest absolute changes would occur for CO_2. Similarly, if the deep ocean affected atmospheric temperatures more prior to 80 years, the effect would apply proportionally to all warming components, possibly strengthening the conclusions here with respect to f.f. BC + OM.

[57] Time-dependent simulations with and without f.f. BC + OM emissions were run because it is difficult to control BC without controlling OM too. For the baseline simulation, emissions of all gas and aerosol species described in sections 2.1 and 2.2, were included, and all processes described in section 2 were solved. Due to the computational burden of the simulations (approximately 35 days of computer time per simulation year), only 5 years of simulation were performed and results were held constant thereafter. For the sensitivity simulation, the only change made was that f.f. BC + OM emissions were removed. Major f.f. sources of BC include hard coal, brown coal, diesel fuel, and jet fuel. The ratios of emitted OM/BC from these fuels are about 1.9:1, 3.9:1, 1:1, and 0.6:1, respectively, giving a weighted ratio of about 2:1 [*Cooke et al.*, 1999] [assuming an OM/OC ratio of 1.3]. The 2:1 ratio was used here when removing OM and BC from f.f. Sulfate now comprises <1% of diesel emissions [*Shauer et al.*, 1999].

[58] Figure 1 shows that, after 5 years of the transient simulation, removing f.f. BC + OM cooled climate by about 0.35 K. The cooling exceeded that from removing CH_4 emissions for all 100 years and CO_2 emissions for 25–100 years (depending on whether CO_2's lifetime was 50 or 200 years). The figure further implies that any emission reduction of f.f. BC + OM would cool climate more than would any emission reduction of CO_2 or CH_4 for a specific period. The period approaches zero in the extreme case of a minute reduction in f.f. BC + OM and a complete reduction in anthropogenic CO_2.

[59] The sum of warming due to anthropogenic CO_2 + CH_4 + f.f. BC + OM was +1.5 K. Other greenhouse gases, if scalable to CO_2, cause +0.4 K warming, bringing the total warming to +1.9 K. Observed warming from 1850 to 2000 is $+0.75 \pm 0.2$ K [*Jones et al.*, 1999]. It is hypothesized that the 1.2 K difference is due primarily to cooling by anthropogenic particles other than f.f. BC + OM, such as sulfate, nitrate, secondary organics, fly ash, soil dust, and reflective anthropogenic biomass-burning particles. Natural climate variations could also be responsible for some of the difference, but the net historic effect between 1860 and 2000 may be small [*Stott et al.*, 2000].

[60] To test the hypothesis that non-BC aerosols cause cooling, time-dependent simulations (accounting for all effects discussed) in which all f.f. SO_2 emissions were and were not included were run. The short-term cooling due to f.f. SO_2 alone was -0.7 K. Further simulations are necessary to elucidate climate responses of other aerosol particle components, but given the magnitude of the atmospheric burdens of these other components, it appears plausible that they could be responsible for the additional cooling.

[61] In sum, the observed 1850–2000 warming can feasibly be reconciled by considering greenhouse gases, f.f. BC + OM, and other particulate, implying that non-BC + OM particulates mask much actual global warming to date. The results here also imply that eliminating all f.f. BC + OM with no other change might reduce >40% (0.35 K/0.75 K) of net global warming to date and >15% (0.35 K/1.9 K) of total global warming before cooling is subtracted out. Based on sensitivity tests, the estimated ranges of these values are 20–45% and 8–18%, respectively. Reducing CO_2 emissions by a third would have the same effect, but over 50–200 years.

[62] The long-term climate responses of reducing emissions calculated here (-0.35 K for f.f. BC + OM, -0.9 K for CO_2, -0.27 K for CH_4, and +0.7 K for SO_2) are within uncertainty ranges of those calculated using a different approach by *Hansen and Sato* [2001]. Their values were -0.38 K for f.f. BC, -1.05 K for CO_2, -0.53 K for CH_4, and +0.75 K for SO_2. Their approach was to estimate a total (direct plus other) forcing for each component and multiply the estimated total forcing by a climate response function, 0.75 K per W/m^2 total forcing.

[63] Another type of climate response function is the climate (K) response per unit direct forcing rather than total forcing. For this study, these functions were 1.4 (0.35 K/0.25 W/m^2), 0.6 (0.9 K/1.6 W/m^2), 0.6 (0.27 K/0.47 W/m^2), and 2 (-0.7 K/-0.35 W/m^2) for f.f. BC + OM, CO_2, CH_4, and SO_2, respectively. The f.f. BC + OM and SO_2 ratios were about 2 and 3 times higher, respectively, than were the CO_2 and CH_4 ratios, because particles have several effects that major greenhouse gases do not (e.g., "indirect effect,"

"self-feedback effect", "semidirect effect", "BC-low-cloud positive feedback loop", photochemistry effect", and "rain-out effect"). SO_2 had a greater climate response (in the opposite direction) than did BC + OM, partly because the "indirect effect" cooled climate in both cases, offsetting some warming in the case of BC + OM and increasing cooling in the case of SO_2. Also, because SO_2 is a gas and spreads further than does BC + OM, the resulting sulfate spread further and had a greater hemispheric "indirect effect" than did BC + OM. Results here indicate that sulfate increased cloud optical depths more than did BC + OM. The 3:1 ratio of sulfate to CO_2 climate response divided by direct forcing is in the range of *IPCC* [2001], who assumes that temperatures are proportional to total forcing and suggest that the ratio of the aerosol indirect "forcing" upper limit plus sulfate direct forcing mean to the sulfate direct forcing mean is 6:1, compared with 1:1 for CO_2.

[64] Results here suggest that BC warmed the air by 360,000–840,000 times more effectively per unit mass than did CO_2, which illustrates why a small mass of BC can have such a large climate effect. In the simulations, the global loading of f.f. BC + OM (where the OM in this term is primary) varied during the year from 0.25 to 0.6 Tg (one-third was f.f. BC and two thirds f.f. OM). The atmospheric loading of anthropogenic CO_2 is approximately 182,000 Tg. Dividing the long-term warming due to f.f. BC + OM (0.35 K) and anthropogenic CO_2 (0.9 K) by their respective loadings and dividing the result for f.f. BC + OM by that for CO_2 gives the warming per unit mass of f.f. BC + OM versus that of CO_2 as 120,000–280,000:1. Multiplying by three (the mass ratio of BC + OM to BC) gives the warming per unit mass of f.f. BC versus that of CO_2 as 360,000–840,000:1.

5. Uncertainties and Comparisons With Observations

[65] Uncertainties in the model include uncertainties in continuous input data (e.g., emission data), model data (e.g., chemical rate coefficient, absorption cross section, aerosol thermodynamic, refractive index, land use, and soil data), model processes, model resolution, and model numerics.

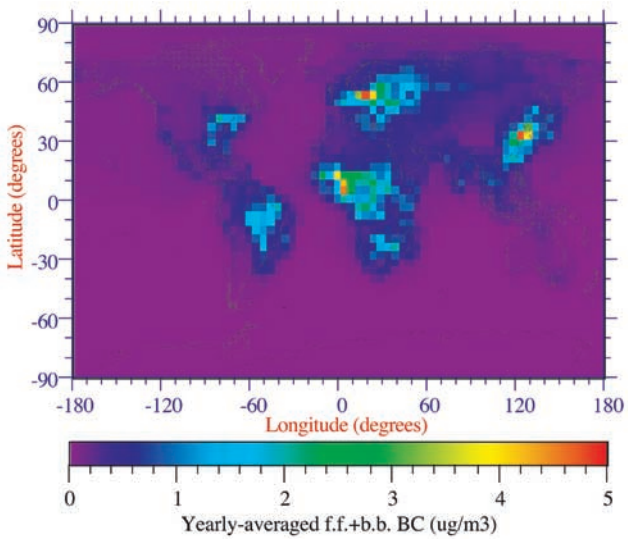

Figure 2. Fifth-year average global distribution of modeled near-surface biomass-burning plus f.f. BC ($\mu g/m^3$), obtained from the baseline simulation.

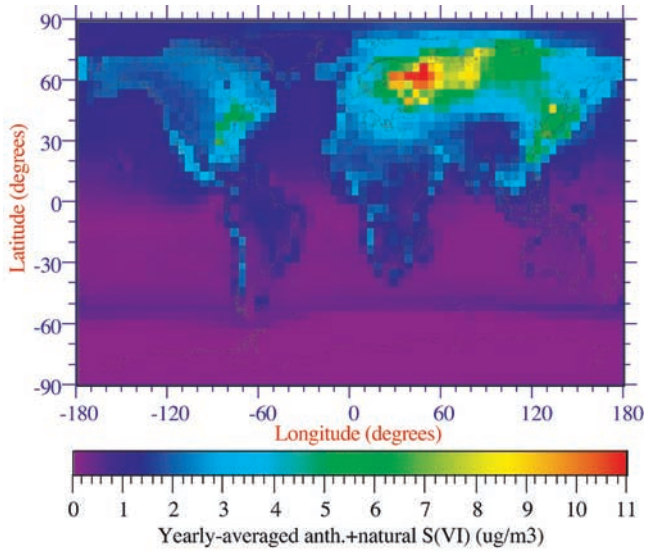

Figure 3. Fifth-year average global distribution of modeled near-surface anthropogenic plus natural S(VI)(aq) ($\mu g/m^3$), obtained from the baseline simulation.

[66] A process that was ignored (in part due to the short simulation period) was long-term natural climate variation. This process would affect predictions over the long term, but should not affect the conclusions here, since, natural variations are expected to affect the climate relatively equally when an anthropogenic component in present and absent.

[67] Another source of uncertainty is random model variability. For example, would the results change if initial conditions changed or a model process was treated differently. To test this, 11 additional simulations with and without f.f. BC + OM were performed, each with a different initial condition, emissions, or treatment of one or more model processes. The simulations resulted in net globally averaged temperature changes due to f.f. BC + OM of +0.15 to +0.5K (compared with the +0.35 K from the baseline case), indicating some variability in predictions of the climate response of f.f. BC + O but in all cases supporting the conclusions found here.

[68] Figure 2 shows modeled near-surface BC concentrations from the baseline simulation. BC sources included biomass burning and f.f. Table 1 compares modeled versus measured near-surface BC. The table indicates that BC concentrations were, on average, slightly higher than observations over marine regions but much lower than observations over many urban areas, where BC concentrations were highest, suggesting that BC warming may be higher than estimated here.

[69] Figure 3 shows modeled near-surface anthropogenic plus natural S(VI) concentrations from the baseline case. Table 2 compares modeled with measured S(VI). S(VI) predictions compared well in many urban and rural areas, but they were low in some of the most polluted areas (e.g., Beijing, Nylsvley, Atlanta, and Po Valley). Sulfate was somewhat overpredicted in a few remote areas and underpredicted in others.

Table 2. Comparison of Modeled Versus Observed Near-Surface Sulfate Concentrations

Station	Latitude	Longitude	Modeled sulfate (ng/m^3)	Measured sulfate (ng/m^3)	Period	Data reference
			Marine			
Atlantic Ocean	31–37°N	66–76°W	2400	1060–540	January–February	*Quinn et al.* [2001]
	15–31°N	43–66°W	550	500–1080		
	8–15°N	33–43°W	560	1760–2490		
	3–8°N	26–33°W	410	890–2400		
	5°S–3°N	17–26°W	250	880–2100		
	25–5°S	6°E–17°W	150	630–1570		
	33–24°S	18–6°E	850	965–1720		
Mawson, Antarctica	68°S	63 °E	30	112	Annual	*Savoie et al.* [1993]
NE Pacific	27–48°N	175°E	1200	500–4000	April–October	*Kaneyasu and Murayami* [2000]
Ny-Alesund, Arctic	78°54′N	11°53′E	1900	516	March–June	*Beine et al.* [2001]
Palmer, Antarctica	65°S	64 °W	45	97	Annual	*Savoie et al.* [1993]
Queen Maud Land, Antarctica	73°3′S	13°25′W	30	228	December–February	*Kerminen et al.* [2000]
San Nicolas Island	33°9′N	119°18′W	2490	1960	Annual	*Kim et al.* [2000]
Tasmania	43°S	144°E	250	155	December	*Berresheim et al.* [1990]
Tropical North Atlantic	13–167°N	60–23°W	1620	260–3670	April	*Johansen et al.* [2000]
West Atlantic	31°N	75°W	2670	3200	January–December	*Berresheim et al.* [1990]
			Rural			
Algoma, Ontario	47°N	84°W	3870	2570	Annual	*McNaughton and Vet* [1996]
Amazon	3°N	69°W	850	315	April–May	*Talbot et al.* [1990]
			1200	485	July–August	
Archbold, Fla.	27°N	81°W	3380	2950	Annual	*McNaughton and Vet* [1996]
Aspvreten, Sweden	58°48′N	17°23′W	1460	1400	June–July	*Zappoli et al.* [1999]
Big Moose, N. Y.	44°N	75°W	4830	3750	Annual	*McNaughton and Vet* [1996]
Brookings, S. D.	44°N	97°W	2120	2190	Annual	*McNaughton and Vet* [1996]
Chapais, Quebec	50°N	75°W	3340	1765	Annual	*McNaughton and Vet* [1996]
Congo	4°N	14°E	935	835	June	*Clairac et al.* [1988]
			1170	1040	October	
Cree Lake, Saskatchewan	57°N	107°W	2040	940	Annual	*McNaughton and Vet* [1996]
Fernberg, Minn.	48°N	91°W	2600	1385	Annual	*McNaughton and Vet* [1996]
Guyana	4°N	58°W	920	250	June	*Gregory et al.* [1986]
Janiskoski, Russia	69°N	29°E	5870	1710	Annual	*Hjellbrekke and Hanssen* [1998]
K-puszta, Hungary	46°57′N	19°42′E	4550	2670	July–August	*Temesi et al.* [2001]
			4550	1400–12,600	July–August	*Zappoli et al.* [1999]
			4000	5760	Annual	*Hjellbrekke and Hanssen* [1998]
Kejimkujik, Nova Scotia	44°N	65°W	3550	2840	Annual	*McNaughton and Vet* [1996]
Maldives	4°58′N	73°28′E	770	2700–9400	February	*Chowdhury et al.* [2001]
Northeast Greenland	81°36′N	16°40′W	1100	490	Annual	*Heidam et al.* [1998]
Nylsvley, South Africa	24°39′N	28°24′E	2650	5890–13,800	May	*Puxbaum et al.* [2000]
Shawano, Wis.	45°N	89°W	3090	3410	Annual	*McNaughton and Vet* [1996]
Winterport, Maine	45°N	69°W	3690	3120	Annual	*McNaughton and Vet* [1996]
Yampa, Colo.	40°N	107°W	1760	1080	Annual	*McNaughton and Vet* [1996]

Table 2. (continued)

Station	Latitude	Longitude	Modeled sulfate (ng/m^3)	Measured sulfate (ng/m^3)	Period	Data reference
			Urban			
Arendtsville, Pa.	40°N	77°W	4600	6773	Annual	*McNaughton and Vet* [1996]
Atlanta, Ga.	33°N	85°W	3500	2000–20,500	August	*Modey et al.* [2001]
Beijing, China	40°N	116°E	3630	14,250	Annual	*He et al.* [2001]
			2790	17,140	Summer	
			3240	12,550	Autumn	
			4330	24,870	Winter	
			4000	10,150	Spring	
Bells, Tenn.	36°N	89°W	4740	5170	Annual	*McNaughton and Vet* [1996]
Bilthoven, Netherlands	52°N	5°E	3630	4400	Annual	*Hjellbrekke and Hanssen* [1998]
Due West, S. C.	34°N	82°W	3900	5840	Annual	*McNaughton and Vet* [1996]
Fort Wayne, Indiana	41°N	85°W	5730	6300	Annual	*McNaughton and Vet* [1996]
Ispra, Italy	46°N	9°E	2860	5600	Annual	*Hjellbrekke and Hanssen* [1998]
Ithaca, N. Y.	42°N	76°W	5070	5000	Annual	*McNaughton and Vet* [1996]
Jarczew, Poland	51°N	22°E	4910	9130	Annual	*Hjellbrekke and Hanssen* [1998]
Jerome, Miss.	38°N	92°W	3910	4130	Annual	*McNaughton and Vet* [1996]
Kosetice, Czech Republic	50°N	15°E	3990	6960	Annual	*Hjellbrekke and Hanssen* [1998]
La Cartuja, Spain	37°N	4°W	2170	4020	Annual	*Hjellbrekke and Hanssen* [1998]
Logrono, Spain	42°N	2°W	2290	3290	Annual	*Hjellbrekke and Hanssen* [1998]
Los Angeles Basin	34°4′N	118°15′W	2330	4240–5190	Annual	*Kim et al.* [2000]
Marion, Ala.	33°N	87°W	4380	5190	Annual	*McNaughton and Vet* [1996]
Marshall, Tex.	33°N	94°W	2760	5110	Annual	*McNaughton and Vet* [1996]
Mountain Lake, Va.	37°N	81°W	3790	6710	Annual	*McNaughton and Vet* [1996]
Pittsboro, N. C.	36°N	79°W	3800	6041	Annual	*McNaughton and Vet* [1996]
Po Valley, Italy	44°39′N	11°37′E	3150	3400–11,000	September	*Zappoli et al.* [1999]
Roquetas, Spain	41°N	1°W	2340	3750	Annual	*Hjellbrekke and Hanssen* [1998]
Suwalki, Poland	54°N	23°E	5730	6220	Annual	*Hjellbrekke and Hanssen* [1998]
Svratouch, Czech Republic	50°N	16°E	4160	5710	Annual	*Hjellbrekke and Hanssen* [1998]
Thessaloniki	40°31′N	22°58′E	4250	4500–8200	June	*Chazette and Liousse* [2001]
Toledo, Spain	40°N	4°W	2200	1820	Annual	*Hjellbrekke and Hanssen* [1998]
Uvalda, Ga.	32°N	82°W	3910	4470	Annual	*McNaughton and Vet* [1996]
Vysokoe, Belarus	52°N	23°E	5150	3960	Annual	*Hjellbrekke and Hanssen* [1998]
Warwick, Mass.	43°N	72°W	4680	4360	Annual	*McNaughton and Vet* [1996]
Witteveen, Netherlands	53°N	7°E	3980	3780	Annual	*Hjellbrekke and Hanssen* [1998]
Zanesville, Ohio	40°N	82°W	4880	6980	Annual	*McNaughton and Vet* [1996]

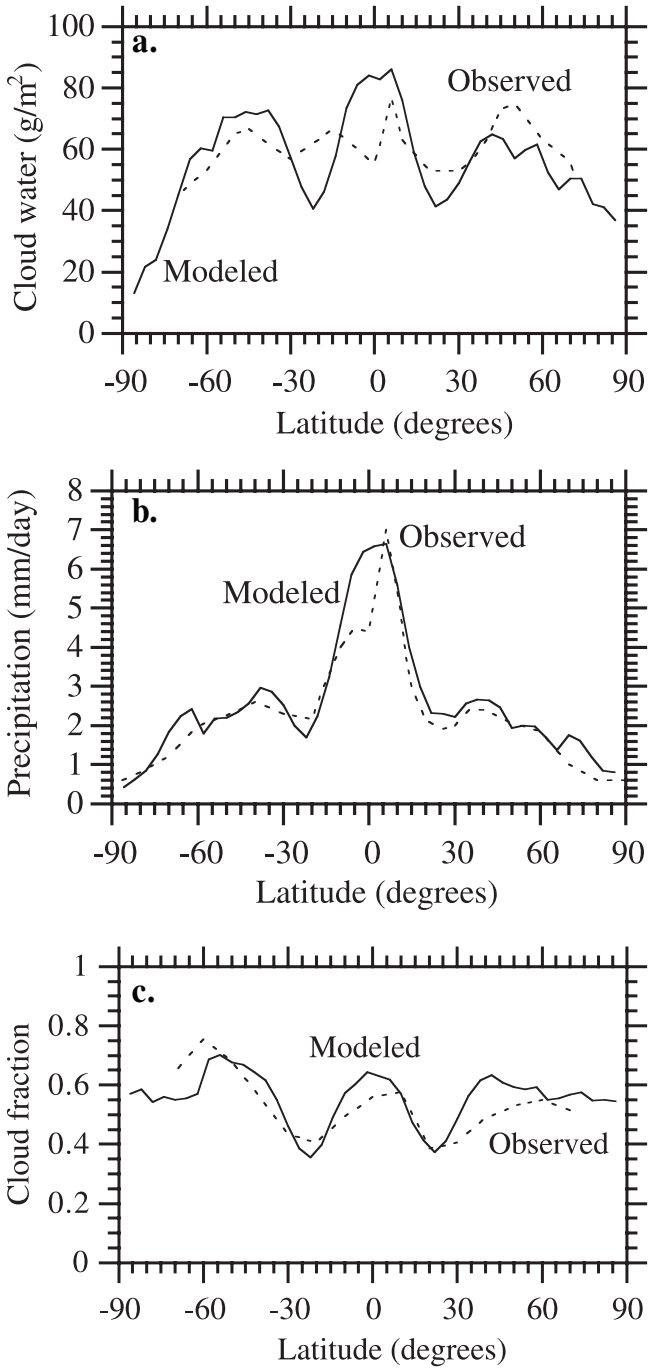

Figure 4. Comparison of yearly and zonally averaged modeled with (a) satellite-derived cloud water [*Greenwald et al.*, 1995], (b) climatological precipitation [*Xie and Arkin*, 1996], and (c) Nimbus-7 satellite cloud fraction data [*Hack et al.*, 1998].

[70] Comparisons of model predictions of direct forcing with those from other studies are given by *Jacobson* [2001b] for several components. Of relevance, the direct forcing per unit mass of organic carbon (OC) (= OM/1.3) was -64 W/m^2/g OC when UV absorption by organics was ignored, consistent with -70 W/m^2/g OC from the work of *Cooke et al.* [1999]. When UV absorption by organics was accounted for, the OC direct forcing was -43 W/m^2/g OC.

[71] Another source of uncertainty is cloud and precipitation fields. Figures 4a–4c compare yearly and zonally averaged cloud water, precipitation, and cloud fraction with satellite-derived or climatological fields. In all cases, the model predicted observed general characteristics. Due in part to the coarse model resolution, much uncertainty still exists in predicting the location, height, water content, and optical characteristics of clouds.

6. Analysis of Climate Response and Individual Effects

[72] Figures 5–14 are difference plots for several variables, all obtained by taking the difference in results in year 5 when f.f. BC + OM emissions were and were not included, respectively. In both cases, BC and all other emissions from biomass burning were included. The only difference between the two simulations was f.f. BC + OM emissions.

[73] Figure 5 shows the difference in near-surface f.f. BC from the two simulations. Most f.f. BC originated from the eastern United States, Europe, eastern Asia, and parts of South America and Africa. Figure 6 shows the difference in year 5 in near-surface temperatures resulting from the f.f. BC + OM simulation. The globally averaged difference was +0.35 K. Most the globe warmed due to BC + OM, but not necessarily in the regions where near-surface BC + OM concentrations were highest. The major regions of warming were over Eastern Russia, Southeast Asia, and Southwestern North America. The major region of cooling was over the North Atlantic. Both the regions of warming and cooling are consistent in location with major observed regions of warming and cooling, respectively, between 1949 and 1997 [*Knutson et al.*, 1999, Plate 3a; *Schneider and Held*, 2001, Figure 1a + c]. The results here account for some of the observed trends even when perturbations to greenhouse gases are not considered, implying that a portion of such observed trends may be due to f.f. BC + OM.

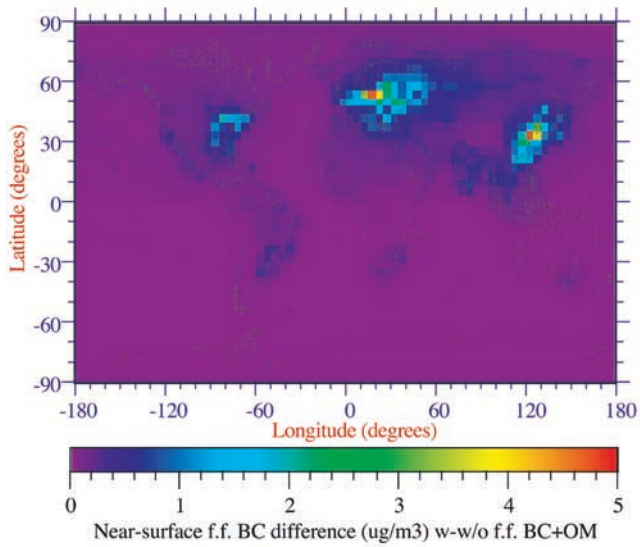

Figure 5. (a) Fifth-year average difference in near-surface f.f. BC concentration (μg/m^3) when f.f. BC + OM emissions were versus were not included in the calculation. (b) Same as (a), but for zonally averaged BC (μg/m^3).

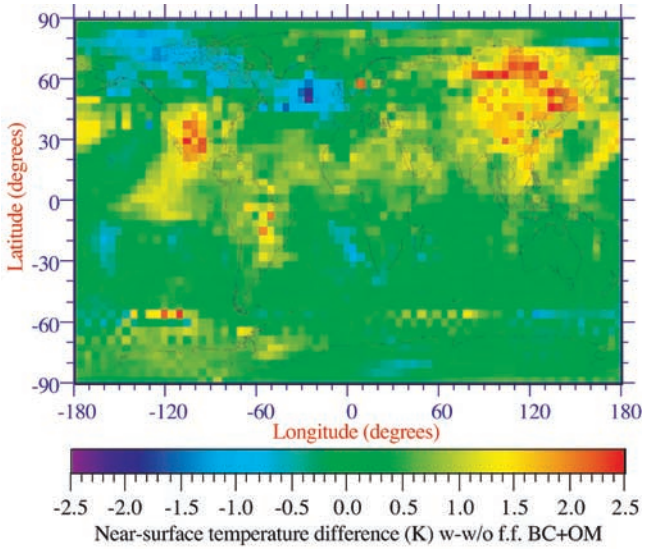

Figure 6. Same as Figure 5a, but for near-surface air temperature (K).

[74] Figure 7a shows the globally and time-averaged layer and cumulative temperature differences after the transient f.f. BC + OM and equilibrium f.f. CO_2 removal simulations. Whereas, f.f. CO_2 and f.f. BC + OM warmed the lower troposphere, CO_2 cooled the upper troposphere and stratosphere (because absorption of thermal-IR by CO_2 in the lower troposphere prevented that thermal-IR from being absorbed in the stratosphere). The maximum cooling from 30 to 100 mb was 1.5 K, which compares with a 1.5–2 K cooling from radiosonde measurements [*Angell*, 1999] due to all climate perturbations at 30–100 mb since 1958. As such, a significant portion of stratospheric cooling since 1958 appears to be due to greenhouse gas buildup in the troposphere. The large modeled decrease in upper stratospheric temperatures found here is supported by *Akmaev and Fomichev* [2000], who used a global model to predict a cooling of 3 K at 50 km when CO_2 was increased from 313 to 360 ppmv. Scaling their cooling by the ratio of the CO_2 change assumed here (280 to 365 ppmv) to that assumed there gives a cooling from their results of 5.4 K, which compares with a cooling here of 5.8 K.

[75] The f.f. BC + OM increased air temperatures relative to ground temperatures (Figure 7a), increasing the stability of near-surface air, slightly slowing near-surface winds, reducing low troposphere and midtroposphere cumulus convection (Figure 7b), increasing low-cloud liquid water (Figure 7c), decreasing middle cloud liquid water and ice and upper cloud ice (Figure 7c), and reducing precipitation (Table 3). Despite overall lower cloud liquid water and ice contents (Table 3 and Figure 7c), the "first indirect effect" increased the 550 nm cloud scattering optical depth at these levels (Figure 7d). Because BC existed within, above, and below cloud layers (e.g., Figure 7e), the enhanced cloud scattering increased solar plus thermal-IR heating within and above clouds up to 250 mb (Figure 7b).

[76] The warming due to BC within the boundary layer and within and above cloud layers increased the downward sensible heat flux to the surface, increasing surface temperatures although not to the same extent as atmospheric temperatures. For example, f.f. BC + OM increased surface temperatures by about 0.28 K, which was 0.07 K less than near-surface air temperatures increased in the global average (Figure 7a). Due to the increases in surface temperatures, more ocean and soil water evaporated, increasing water vapor contents (Figure 7d). Increases in tropospheric and lower stratospheric water vapor is an observed trend [*Oltmans and Hofmann*, 1995]. Since the air was warmer, saturation vapor pressures were higher, allowing more water vapor to accumulate and reducing cloud liquid, cloud ice, and precipitation in the global average (Table 3). The accumulation of water vapor increased solar-IR and thermal-IR heating rates, increasing air temperatures further ("BC-water vapor positive feedback").

[77] Figure 7e shows the change in globally averaged vertical profiles of BC, S(VI), Na^+, and soil dust resulting when f.f. BC + OM was emitted. The figure shows that f.f. BC + OM increased sodium and sulfate but decreased soil dust. Sulfate and sodium increased partly because precipitation decreased over the oceans and over northern latitudes, where these species were abundant ("rainout effect"). Soil dust decreased, possibly due to the "daytime stability" and "smudge-pot effects" and to the fact that precipitation did not decrease so much over soil dust source regions (deserts). The figure also shows that increases in BC and S(VI) concentrations exceeded those at the surface, suggesting that these components were removed more readily near the surface than aloft by rainout, dry deposition, and sedimentation. For example, rainout from low-lying stratus producing drizzle diminish aerosols near the surface but not above the stratus.

[78] Figure 7g shows the difference in downward minus upward solar, thermal-IR, and total irradiance (total forcing) from the f.f. BC + OM simulations. The solar irradiance difference was positive at the tropopause and negative at the surface, indicating in part that BC and the additional water vapor it produced absorbed solar and solar near-IR radiation, respectively. The reduced downward (increased upward) thermal-IR forcing at the tropopause resulted in part because f.f. BC + OM reduced middle and upper tropospheric cloud liquid water and ice, reducing the downward flux of thermal-IR because liquid water and ice are thermal-IR absorbers. Downward thermal-IR irradiance decreased less at lower altitudes, in part because water vapor and cloud liquid contents increased most down there.

[79] The positive net solar plus thermal-IR tropopause forcing due to f.f. BC + OM is partly explained as follows. BC absorbed sunlight, heating the air (positive forcing). BC + OM increased water vapor, enhancing positive forcing more. BC + OM increased the number of CCN, increasing negative forcing through the "indirect effects", but it reduced middle and upper (and overall) cloud liquid water and ice contents, offsetting some of this negative forcing. The enhanced scattering due to the "first indirect effect" enhanced absorption by BC, H_2O, and CO_2, within and above clouds, increasing positive forcing. BC + OM also reduced surface albedo (Table 3), increasing positive forcing.

[80] A comparison of the positive net forcing due to f.f. BC + OM with estimates of negative "indirect" forcing is a comparison of apples and oranges. The net forcing here is due to direct forcing plus a multitude of time-dependent

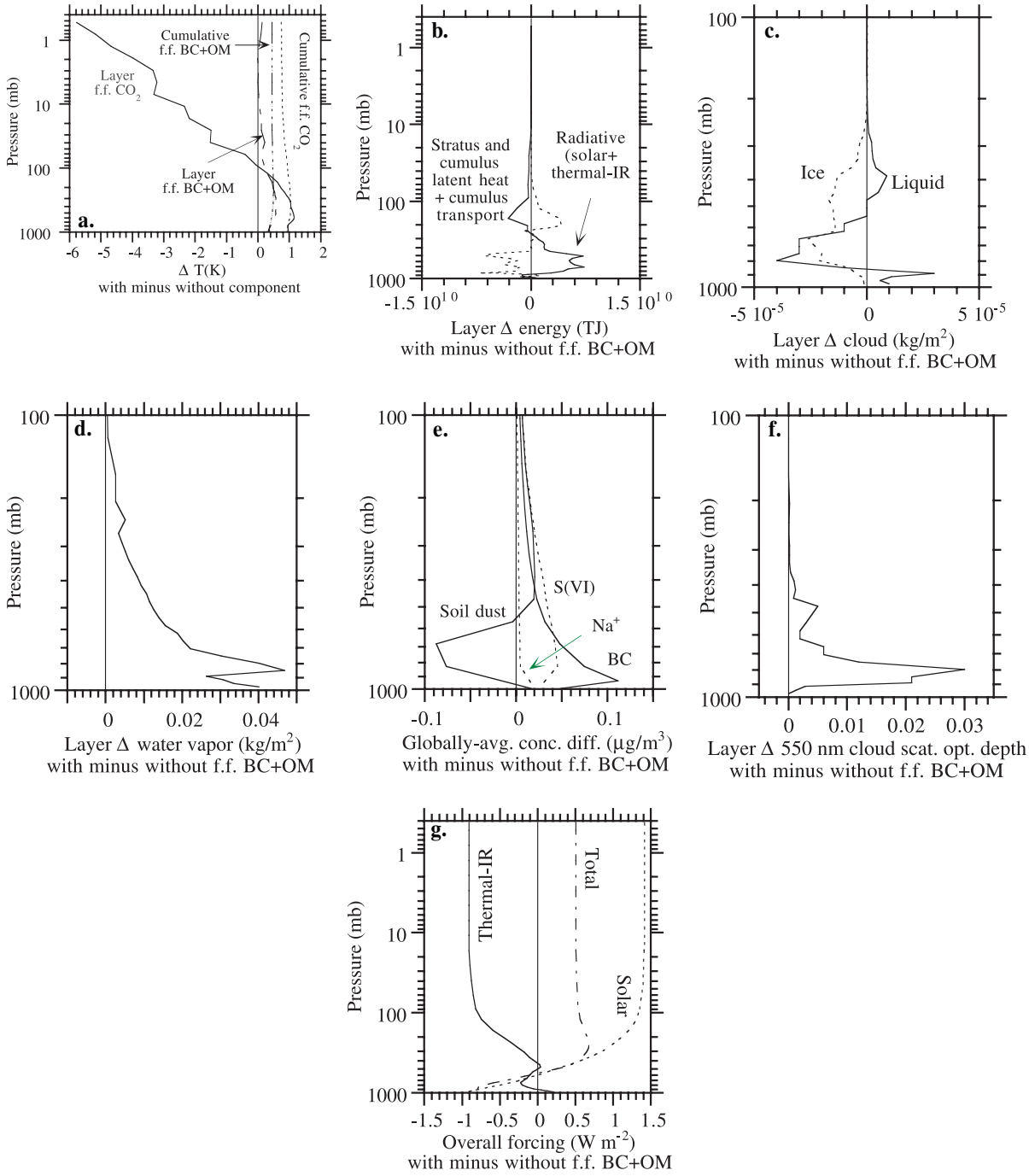

Figure 7. (a) Difference in globally and time-averaged layer and cumulative temperatures when all aerosols and gases were present versus when f.f. BC + OM emissions were removed (transient simulation) and anthropogenic CO_2 above 280 ppmv was removed (equilibrium simulation). The globally and time-averaged temperature of a layer is $T_{layer} = \sum_{c,t} V_{c,t}\rho_{a,c,t}c_{p,a}T_{c,t} / \sum_c V_{c,t}\rho_{a,c,t}c_{p,a}$, where the summation is over all grid cells in the layer and over all time steps during the averaging period, $V_{c,t}$ is the volume of a grid cell at a given time step, $\rho_{a,c,t}$ is the air density in a grid cell at a given time step, $c_{p,a}$ is the specific heat of air at constant pressure, and $T_{c,t}$ is the temperature in a grid cell at a given time step. The cumulative temperature uses a similar equation, except that the integration includes all grid cells from the ground to the altitude of interest. Thus, the cumulative temperature at the stratopause is the integration of air temperature from the surface to the stratopause. The bottom-most "layer" temperature changes are ground-temperature changes, which are not included in the cumulative temperature change curves. The remaining curves are global differences from the simulations with minus without f.f. BC + OM for (a) changes in energy due to latent heat release plus cumulus energy transport and solar plus thermal-IR heating, (b) cloud liquid and ice, (c) cloud scattering optical depth, (d) several aerosol constituents, (e) water vapor, and (f) net downward minus upward solar, thermal-IR, and total irradiance.

Table 3. Fifth-Year Globally Averaged Difference in Several Parameters Resulting From the Simulations When f.f. BC + OM Emissions Were Versus Were Not Included

Parameter	Difference	Parameter	Difference
Near-surface temperature	+0.35 K	Near-surface aerosol single-scattering albedo	−0.029 (−)
Near-surface relative humidity	−0.0017 (out of 1)	Near-surface aerosol LWC	+0.17 μg/m^3
Surface pressure	−0.0003 mb	Near-surface BC	+0.11 μg/m^3
Surface albedo	−0.0017 (out of 1)	Near-surface OM	+0.23 μg/m^3
Cloud optical depth	+0.27 (−)	Near-surface S(VI)	+0.052 μg/m^3
Cloud liquid water	−0.000089 kg/m^2	Near-surface NO_3^-	+0.003 μg/m^3
Cloud ice	−0.00019 kg/m^2	Near-surface Cl^-	+0.004 μg/m^3
Precipitation	−0.017 mm/day	Near-surface NH_4^+	+0.011 μg/m^3
Tropopause total sol + IR forcing	+0.53 W/m^2	Near-surface Na^+	+0.0025 μg/m^3
Aerosol optical depth	+0.023 (−)	Near-surface SO_2	+0.0089 ppbv

effects, including indirect effects, when all effects are linked together. Estimates of indirect forcing, which range from 0 to −2 W/m^2 [*IPCC*, 2001] are based on simulations in which forcing is ascribed to indirect effects only and not to direct effects of f.f. BC + OM nor the effects of the multitude of feedbacks treated here. Nevertheless, the facts that (1) cloud scattering optical depths increased at all altitudes when f.f. BC + OM was included (Figure 7d) and (2) that the inclusion of f.f. BC + OM reduced the mean cloud radius in the global average suggest that indirect forcing here due to f.f. BC + OM was negative. In addition, the total forcing obtained for the with/without f.f. SO_2 simulations was negative, indicating again that indirect forcing must have been negative. It is impossible to isolate the magnitude of indirect forcing without holding many parameters constant, thereby changing the climate responses and rendering the results incorrect (section 3.13), so this was not attempted here.

[81] Figure 8 shows the globally distributed change in near-surface S(VI)(aq) due to the emission of f.f. BC + OM. The increase in particle surface area over western Europe due to f.f. BC + OM appears to have enhanced condensation of H_2SO_4(g), increasing aerosol liquid water content, ammonia uptake (Figure 9), and aqueous oxidation of SO_2 to S(VI)(aq) (all "self-feedback effects"). Because more S(VI)(aq) was produced in western Europe, less was produced in northeastern Europe (Figure 8). At the same time, precipitation decreased over western Europe, decreasing the removal of S(VI)(aq) and SO_2 ("rainout effect"), so it is not clear the extent to which the enhanced S(VI)(aq) over western Europe was due to the "self-feedback effect" versus the "rainout effect."

[82] Figure 10 shows the change in aerosol optical depth (integrated from the surface to top-of-atmosphere) due to the emission of f.f. BC + OM. Aerosol optical depth increased particularly in the Northern Hemisphere, not only due to the addition of f.f. BC + OM but also due to resulting increases in S(VI)(aq), NO_3^-, Cl^-, NH_4^+, Na^+, and aerosol liquid water (Table 3). The greater number concentration of particles (mainly f.f. BC + OM and homogeneously nucleated S(VI)(aq), decreased effective cloud radii and increased cloud optical depths, particularly over Europe and parts of Asia (Figure 11). The change in cloud optical depths reflects the sum of "indirect effects", the "semi-direct effect", and the "BC-low-cloud positive feedback loop". The fact that cloud optical depths increased in the

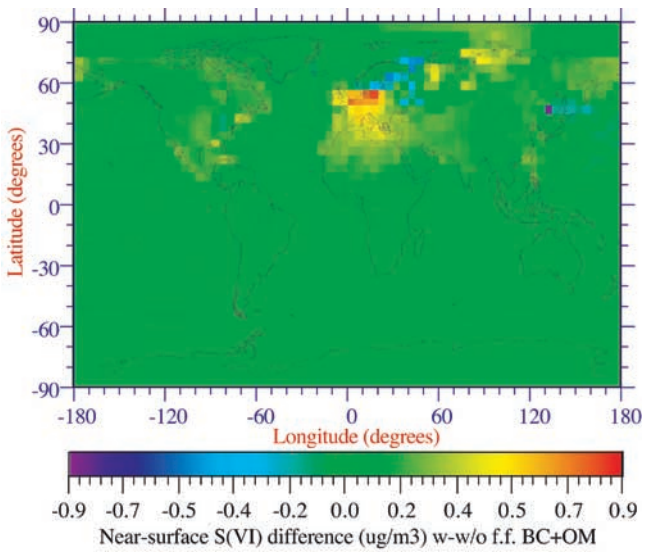

Figure 8. Same as Figure 5a, but for near-surface aerosol S(VI) (μg/m^3).

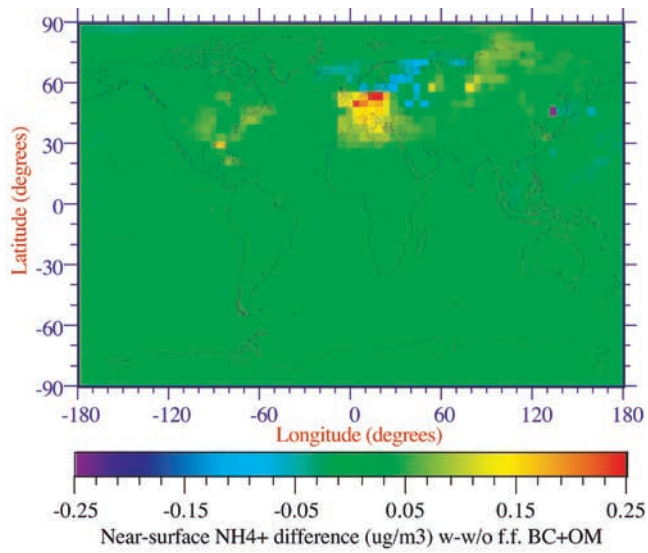

Figure 9. Same as Figure 5a, but for near-surface aerosol NH_4^+ (μg/m^3).

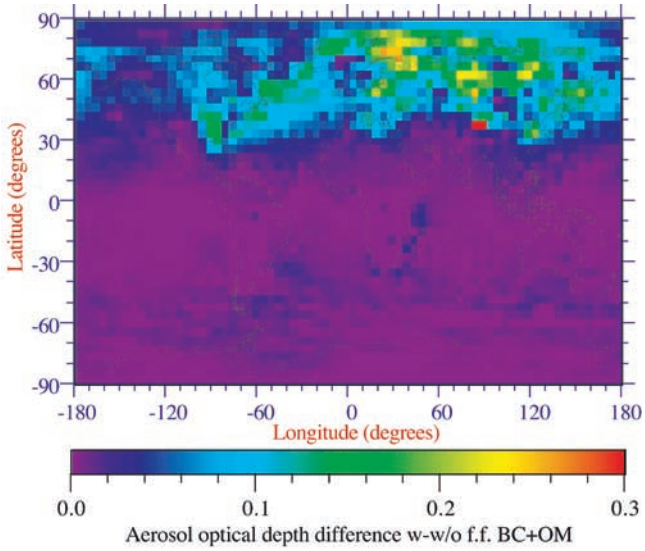

Figure 10. Same as Figure 5a, but for aerosol optical depth.

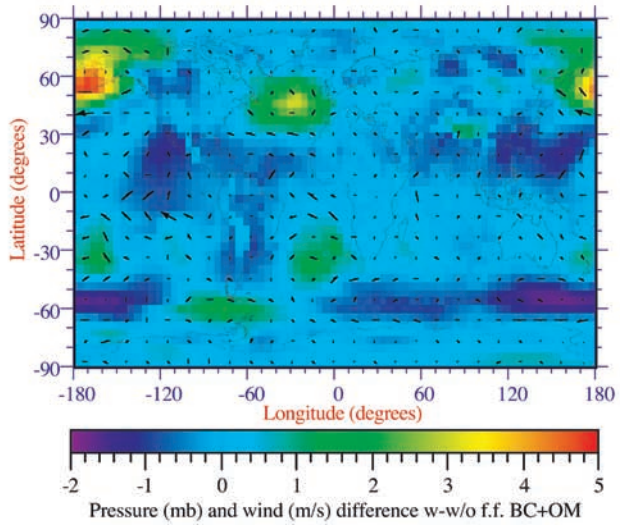

Figure 12. Same as Figure 5a, but for surface pressure (mb) and winds (m/s).

global average (Table 3) suggests that "indirect effects" may have dominated the other two.

[83] Figure 12 shows the change in surface pressures and winds. Changes in winds and pressures affected not only temperatures ("particle effect through large-scale meteorology"), but also clouds and precipitation (Table 3). Changes in winds also affected the emission rates of sea-spray and the Na^+ it contains (Figure 13). The change in Na^+ affected the liquid water content of such drops. For example, a decrease in sodium in the Norwegian Sea decreased aerosol liquid water content noticeably there.

[84] In the global average, the addition of f.f. BC + OM decreased surface albedo (Table 3) primarily due to a slight reduction in Northern Hemisphere land-snow cover (mostly over eastern Russia and Canada. The decreases over eastern Russia coincided with the increase in temperatures there, although it cannot be determined whether the change in albedo caused the change in temperature or vice versa or both.

[85] Finally, in the simulations in which f.f. SO_2 emissions were and were not included, the northeast United States, central and eastern Europe, and much of eastern Asia cooled. Warming occurred over much of the Southern Hemisphere, but was smaller than Northern Hemisphere cooling. A reason for the overall cooling was the effect of f.f. SO_2 emissions on cloud optical depth. Cloud optical depth increased when f.f. SO_2 emissions were included, because f.f. SO_2 produced sulfuric acid–water aerosol particles, which enhanced the "indirect effects". The change in cloud optical depth due to f.f. SO_2 was greater than that due to f.f. BC + OM, partly explaining why the magnitude of the climate response due to f.f. SO_2 was greater than that due to f.f. BC + OM. The cloud optical depth resulting from f.f.

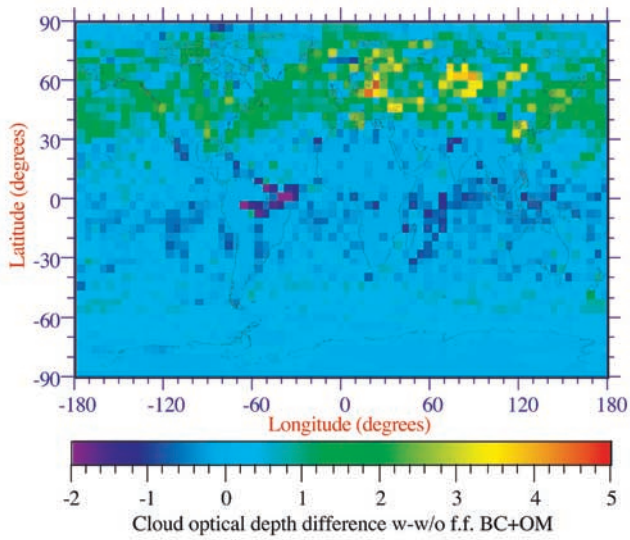

Figure 11. Same as Figure 5a, but for cloud optical depth.

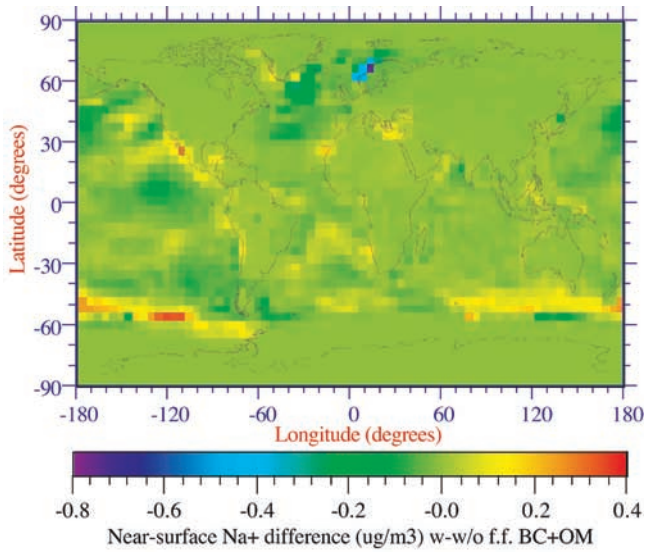

Figure 13. Same as Figure 5a, but for near-surface aerosol Na^+ ($\mu g/m^3$).

SO_2 was greater than that due to f.f. BC + OM, because f.f. SO_2, spread further in the Northern Hemisphere than did f.f. BC + OM (e.g., Figure 3 versus Figure 2). As such, f.f. SO_2 affected clouds over a greater global area than did f.f. BC + OM. The total (direct plus other) forcing resulting from the SO_2 simulations was negative, indicating that the forcing due to the "indirect effects", if they could be isolated, must also have been negative.

7. Comparison of Diesel Versus Gasoline

[86] Two practical strategies to reduce BC + OM are to improve particle traps for diesel vehicles and to replace diesel with gasoline. A modern diesel direct injection (DDI) engine obtains 25–35% better mileage than an equivalent port fuel injection (PFI) gasoline engine, but much of this gain is offset, since diesel releases 18.1% more CO_2 per unit volume than does gasoline [*Wang*, 1999]. Although light-duty diesel engines release less CO_2 than do PFI gasoline engines, they release up to 0.08 g particulates/mi (0.05 g/km) under current U.S. and E.U. emission standards. Most particulate emissions are BC + OM [*Shauer et al.*, 1999; *Lighty et al.*, 2000]. New PFI engines produce 25 to >200 times less particulate mass per distance driven than new DDI engines [*Maricq et al.*, 1999b].

[87] If a new PFI gasoline engine obtains 25 mpg (10.6 km/l), it releases about 95.4 g C/mi (59.4 g C/km) as CO_2 (with gasoline density of 737 g/l and carbon content of 85.5%) [*Wang*, 1999]. An equivalent DDI engine with 30% better mileage obtains 32.5 mpg (13.8 km/l), releasing 86.7 g C/mi (54.0 g C/km) as CO_2 (assuming diesel density of 856 g/l and carbon content of 87.0%) [*Wang*, 1999]. Thus, the DDI engine releases 8.7 g C/mi (9.1%) less CO_2-C than does the PFI engine but 0.08 g C/mi more BC + OM, giving a ratio of CO_2-C saved to BC + OM produced of 109:1. Figure 14 shows that, for a diesel vehicle to cool climate over 1 year, the ratio of CO_2-C saved to BC + OM produced must exceed 5000–21,000:1, which is possible only if BC + OM emissions are reduced to 0.0004–0.0017 g/mi. For diesel to cool over 100 years, the ratio must exceed 220–500:1, which is possible only if BC + OM emissions are reduced to 0.02–0.04 g/mi. In sum, if the calculations here are correct, light-duty diesel cars meeting today's particulate standards and used daily will warm climate during the next 100+ years more than will gasoline cars.

[88] By 2005, E.U. particulate emission standards for light-duty vehicles will decrease to 0.025 g/km (0.04 g/mi). If all cars emitted at this limit, diesel would still warm climate more than would gasoline over a 100 year period (Figure 14). By 2004, California will implement Low Emission Vehicle (LEV) II standards for particulates of 0.01 g/mi (0.006 g/km) [the United States will implement a Tier II standard of up to 0.02 g/mi (0.012 g/km)]. If the tough California standards could be implemented worldwide, diesel would still warm climate more than would gasoline over a period of 13–54 years (Figure 14).

[89] In the United States and Europe, 99% of heavy-duty trucks and buses run on diesel. In the United States, <0.1% of light-duty vehicles run on diesel; in Europe, >25% run on diesel [*Cohen and Nikula*, 1999] (32.3% of new European cars in 2000 were diesel). Despite few U.S. diesel passenger vehicles, diesel consumption rates from all ground transportation sources (road, rail, inland waterways) in the United States are about 75–80% of those in Europe [*International Energy Agency*, 1999]. Table 4 shows that excise tax laws in all E.U. countries except the U.K. favor diesel, inadvertently promoting global warming. Some countries, (e.g., Finland, the Netherlands, Norway, and Sweden) also levy carbon taxes based on the carbon content of fuels. These taxes also favor diesel, since diesel releases less carbon per mile than does gasoline, but we calculate that the small release of BC + OM by diesel warms climate over 100 years than does the extra CO_2 released by gasoline.

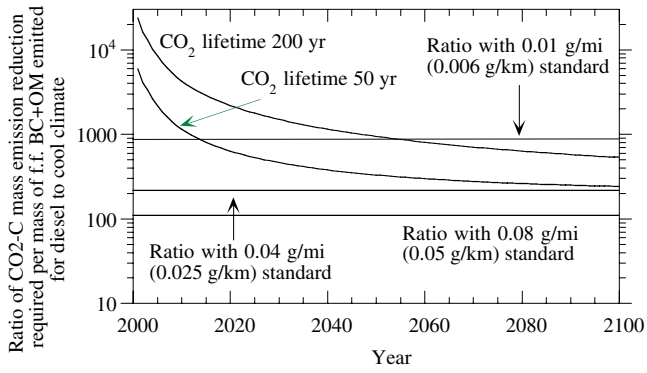

Figure 14. Ratio of CO_2-C mass emission reduction required per mass of f.f. BC + OM emitted for diesel to cool climate. The curves were obtained by dividing the f.f. BC + OM temperature curve in Figure 1 by each CO_2 temperature curve [CO_2 (50 years) and CO_2 (200 years)] then multiplying the result by the current yearly emission rate of CO_2 (8100 Tg C/yr) and dividing by that of BC and associated OM from f.f. (5.1 Tg/yr BC + 10.1 Tg/yr OM). The figure shows that a yearly 1 Tg/yr decrease in f.f. BC + OM emissions will cool climate by 5000–21,000 times more than will a 1 Tg/yr decrease in CO_2-C emissions during 1 year. After 100 years of continuous 1 Tg/yr decreases in both, the resulting ratio of f.f. BC + OM to CO_2-C cooling is 220–500:1. Also shown (straight lines) are the ratios of CO_2-C saved to f.f. BC + OM emitted for a modern diesel vehicle emitting 0.08, 0.04, and 0.01 g/mi BC + OM. The intersection of each of these straight lines with the two curves indicates the period of time during which diesel vehicles enhance global warming more than do gasoline vehicles under the given emission standard. In the case of the 0.08 and 0.04 g/mi standards, the period of time is >100 years.

8. Conclusion

[90] Global model calculation in which 12 identifiable effects of aerosol particles on climate were accounted for were run. Results suggest that any emission reduction of f.f. BC + OM will slow global warming more than will any emission reduction of CO_2 or CH_4 for a specific period. When all f.f. BC + OM and anthropogenic CO_2 and CH_4 emissions are eliminated together, that period is 25–100 years. Historical net global warming can be attributed roughly to greenhouse gas plus f.f. BC + OM warming minus cooling due to other anthropogenic particles. Eliminating all f.f. BC + OM could eliminate 20–45% of such net warming (8–18% of total warming before cooling is

Table 4. Excise Taxes on Diesel and Gasoline in 1997 [*European Commission*, 1997]

	Excise tax on unleaded gasoline (ECU/1000 L)	Excise tax on diesel fuel (ECU/1000 L)	Ratio of tax on gasoline to tax on diesel
Belgium	510	292	1.75:1
Finland	536	310	1.73:1
Sweden	503	298	1.69:1
Netherlands	531	320	1.66:1
France	576	358	1.61:1
Germany	505	321	1.57:1
Denmark	447	308	1.45:1
Greece	363	252	1.44:1
Austria	416	291	1.43:1
Portugal	469	327	1.43:1
Spain	363	264	1.38:1
Italy	534	390	1.37:1
Luxembourg	349	254	1.37:1
Ireland	395	343	1.15:1
UK	501	501	1.00:1

subtracted out) within 3–5 years if no other change occurred. Reducing CO_2 emissions by a third would have the same effect, but after 50–200 years.

[91] Calculations also suggest diesel cars emitting continuously under the most recent U.S. and E.U. particulate standards may warm climate per distance driven over the next 100+ years more than do equivalent gasoline cars. If the estimates here are correct, fuel and carbon tax laws that favor diesel promote global warming. Toughening particulate emission standards to 0.006 g/km (0.01 g/mi), which is planned for California by 2004, does not change the conclusion, but it shortens the period over which diesel causes net warming to 13–54 years.

[92] Other practical strategies for reducing BC + OM are to phase out indoor biomass and coal burning and to improve particle collection from jet fuel and coal burning. Reducing BC + OM will not only slow global warming, but also improve human health. There may be no low threshold for health problems and mortality related to particles [*Pope and Dockery*, 1999], and about 2.7 million people die yearly from air pollution [*WHO*, 2000], many from indoor burning of biomass and coal and outdoor particles. In industrialized countries, the health costs of particulate matter are estimated to be $200,000 to $2.75 million per ton, making particles the most costly components of air pollution [*Spadaro and Rabl*, 2001]. Control of f.f. BC + OM alone will not eliminate long-term global warming. Elimination requires emission reductions in CO_2 and other greenhouse gases as well.

[93] **Acknowledgments.** This work was supported by the NASA New Investigator Program in Earth Sciences, the Environmental Protection Agency, the National Science Foundation, and the David and Lucile Packard Foundation and the Hewlett-Packard Company. I would also like to thank Don Wuebbles, Jim Hansen, Greg Carmichael, Matti Maricq, David Streets, Carey Jang, and John Bachmann for helpful comments and discussions.

References

Ackerman, A. S., B. Toon, D. E. Stevens, A. J. Heymsfield, V. Ramanathan, and E. J. Welton, Reduction of tropical cloudiness by soot, *Science*, *288*, 1042–1047, 2000.

Ackerman, T. P., A model of the effect of aerosols on urban climates with particular applications to the Los Angeles basin, *J. Atmos. Sci.*, *34*, 531–546, 1977.

Albrecht, B. A., Aerosols, cloud microphysics, and fractional cloudiness, *Science*, *245*, 1227–1230, 1989.

Allison, I., R. E. Brandt, and S. G. Warren, East Antarctic sea ice: Albedo, thickness distribution, and snow cover, *J. Geophys. Res.*, *98*, 12,417–12,429, 1993.

Andreae, M. O., and P. Merlet, Emission of trace gases and aerosols from biomass burning, *Global Biogeochem. Cycles*, *15*(4), doi:10.1029/2000GB001382, 2002.

Andreae, M. O., T. W. Andreae, R. J. Ferek, and H. Raemdonck, Long range transport of soot carbon in the marine atmosphere, *Sci. Total Environ.*, *36*, 73–80, 1984.

Andres, R. J., and A. D. Kasgnoc, A time-averaged inventory of subaerial volcanic sulfur emissions, *J. Geophys. Res.*, *103*, 25,251–25,261, 1998.

Angell, J. K., Comparison of surface and tropospheric temperature trends estimated from a 63-station radiosonde network, 1958–1998, *Geophys. Res. Lett.*, *26*, 2761–2764, 1999.

Akmaev, R. A., and V. I. Fomichev, A model estimate of cooling in the mesosphere and lower thermosphere due to the CO_2 increase over the last 3–4 decades, *Geophys. Res. Lett.*, *27*, 2113–2116, 2000.

Arakawa, A., and V. R. Lamb, A potential enstrophy and energy conserving scheme for the shallow water equations, *Mon. Weather Rev.*, *109*, 18–36, 1981.

Beine, H., I. Allegrini, R. Sparapani, A. Ianniello, and F. Valentini, Three years of springtime trace gas and particle measurements at Ny-Alesund, Svalbard, *Atmos. Environ.*, *35*, 3645–3658, 2001.

Berresheim, H., M. O. Andreae, G. P. Ayers, R. W. Gillett, J. T. Merrill, V. J. Davis, and W. L. Chameides, Airborne measurements of dimethlylsulfide, sulfur dioxide, and aerosol ions over the Southern Ocean south of Australia, *J. Atmos. Chem.*, *10*, 341–370, 1990.

Bergstrom, R. W., and R. Viskanta, Modeling of the effects of gaseous and particulate pollutants in the urban atmosphere, part I, Thermal structure, *J. Appl. Meteorol.*, *12*, 901–912, 1973.

Berner, A., S. Sidla, Z. Galambos, C. Kruisz, R. Hitzenberger, H. M. ten Brink, and G. P. A. Kos, Modal character of atmospheric black carbon size distributions, *J. Geophys. Res.*, *101*, 19,559–19,565, 1996.

Bhugwant, C., H. Cachier, M. Bessafi, and J. Leveau, Impact of traffic on black carbon aerosol concentration at la Reunion Island (Southern Indian Ocean), *Atmos. Environ.*, *34*, 3463–3473, 2000.

Boccippio, D. J., K. L. Cummins, H. J. Christian, and S. J. Goodman, Combined satellite- and surface-based estimation of the intracloud-cloud-to-ground lightning ratio over the continental United States, *Mon. Weather Rev.*, *129*, 108–122, 2001.

Bouwman, A. F., D. S. Lee, W. A. H. Asman, F. J. Dentener, K. W. van der Hoek, and J. G. J. Olivier, A global high-resolution emission inventory for ammonia, *Global Biogeochem. Cycles*, *11*, 561–587, 1997.

Brémond, M. P., H. Cachier, and P. Buat-Ménard, Particulate carbon in the Paris region atmosphere, *Environ. Technol. Lett.*, *10*, 339–346, 1989.

Bretherton, C. S., E. Klinker, A. K. Betts, and J. Coakley, Comparison of ceilometer, satellite, and synoptic measurements of boundary layer cloudiness and the ECMWF diagnostic cloud parameterization scheme during ASTEX, *J. Atmos. Sci.*, *52*, 2736–2751, 1995.

Brorström-Lundén, E., A. Lindskog, and J. Mowrer, Concentrations and fluxes of organic compounds in the atmosphere of the Swedish west coast, *Atmos. Environ.*, *28*, 3605–3615, 1994.

Brunciak, P. A., J. Dachs, T. P. Franz, C. L. Gigliotti, E. D. Nelson, B. J. Turpin, and S. J. Eisenreich, Polychlorinated biphenyls and particulate organic/elemental carbon in the atmosphere of Chesapeake Bay, USA, *Atmos. Environ.*, *35*, 5663–5677, 2001.

Cachier, H., P. Buat-Ménard, M. Fontugne, and R. Chesselet, Long-range transport of continentally-derived particulate carbon in the marine atmosphere: Evidence from stable carbon isotope studies, *Tellus*, *38B*, 161–177, 1986.

Cachier, H., M-P. Brémond, and P. Buat-Ménard, Determination of atmospheric soot carbon with a simple thermal method, *Tellus*, *41B*, 379–390, 1989.

Cachier, H., M.-P. Brémond, and P. Buat-Ménard, Organic and black carbon aerosols over marine regions of the Northern Hemisphere, in *Proceedings of the International Conference on Atmospheric Chemistry*, edited by L. Newman et al., pp. 249–261, Brookhaven Natl. Lab., Upton, N. Y., 1990.

Cachier, H., C. Liousse, A. Cachier, B. Ardouin, G. Polian, V. Kazan, and A. D. A. Hansen, Black carbon aerosols at the remote site of Amsterdam Island, in *Fifth International Conference on Carbonaceous Aerosols*, U.S. Dept. of Energy, Berkeley, Calif., 23–26 August 1994.

Chazette, P., and C. Liousse, A case study of optical and chemical ground apportionment for urban aerosols in Thessaloniki, *Atmos. Environ.*, *35*, 2497–2506, 2001.

Chowdhury, Z., L. S. Hughes, L. G. Salmon, and G. R. Cass, Atmospheric

particle size and composition measurements to support light extinction calculations over the Indian Ocean, *J. Geophys. Res.*, *106*, 28,597–28,605, 2001.

Chylek, P., C. M. Banic, B. Johnson, P. A. Damiano, G. A. Isaac, W. R. Leaitch, P. S. K. Liu, F. S. Boudala, B. Winter, and D. Ngo, Black carbon: Atmospheric concentrations and cloud water content measurements over southern Nova Scotia, *J. Geophys. Res.*, *101*, 29,105–29,110, 1996.

Clairac, B., R. Delmas, B. Cros, H. Cachier, P. Buat-Menard, and J. Servant, Formation and chemical composition of atmospheric aerosols in an equatorial forest area, *J. Atmos. Chem.*, *6*, 301–322, 1988.

Clarke, A. D., Aerosol light absorption by soot in remote environments, *Aerosol. Sci. Technol.*, *10*, 161–171, 1989.

Clarke, A. D., R. E. Weiss, and R. J. Charlson, Elemental carbon aerosols in the urban, rural, and remote-marine troposphere and in the stratosphere: Inferences from light absorption data and consequences regarding radiative transfer, *Sci. Total Environ.*, *36*, 97–102, 1984.

Cohen, A. J., and K. Nikula, The health effects of diesel exhaust: Laboratory and epidemiologic studies, in *Air Pollution And Health*, edited by S. T. Holgate et al., pp. 707–745, Academic, San Diego, Calif., 1999.

Cooke, W. F., and J. J. N. Wilson, A global black carbon aerosol model, *J. Geophys. Res.*, *101*, 19,395–19,409, 1996.

Cooke, W. F., C. Liousse, H. Cachier, and J. Feichter, Construction of a 1° × 1° fossil fuel emission data set for carbonaceous aerosol and implementation and radiative impact in the ECHAM4 model, *J. Geophys. Res.*, *104*, 22,137–22,162, 1999.

Del Delumyea, R., and A. Kalivretenos, Elemental carbon and lead content of fine particles from American and French cities of comparable size and industry, 1985, *Atmos. Environ.*, *21*, 1643–1647, 1987.

Derwent, R. G., D. B. Ryall, S. G. Jennings, T. G. Spain, and P. G. Simmonds, Black carbon aerosol and carbon monoxide in European regionally polluted air masses at Mace Head, Ireland during 1995–1998, *Atmos. Environ.*, *35*, 6371–6378, 2001.

Dickerson, R. R., S. Kondragunta, G. Stenchikov, K. L. Civerolo, B. G. Doddridge, and B. N. Holben, The impact of aerosols on solar ultraviolet radiation and photochemical smog, *Science*, *278*, 1997.

Didyk, B. M., B. R. T. Simoneit, L. A. Pezoa, M. L. Riveros, and A. A. Flores, Urban aerosol particles of Santiago, Chile: Organic content and molecular characterization, *Atmos. Environ.*, *34*, 1167–1179, 2000.

Ding, P., and D. A. Randall, A cumulus parameterization with multiple cloud-base levels, *J. Geophys. Res.*, *103*, 11,341–11,353, 1998.

Dzubay, T. G., R. K. Stevens, and P. L. Haagenson, Composition and origins of aerosol at a forested mountain in Soviet Georgia, *Environ. Sci. Technol.*, *18*, 873–883, 1984.

European Commission, Vehicle taxation in the European Union 1997, *European Commission Directorate General XXI, background paper Ref XXI/306/98-EN*, 1997.

Ferek, R. J., J. S. Reid, P. V. Hobbs, D. R. Blake, and C. Liousse, Emission factors of hydrocarbons, halocarbons, trace gases and particles from biomass burning in Brazil, *J. Geophys. Res.*, *103*, 32,107–32,118, 1998.

Food and Agricultural Organization (FAO), *Soil Map of the World*, Land and Water Dev. Div., FAO, Rome, Italy, 1995.

Greenwald, T. J., G. L. Stephens, S. A. Christopher, and T. H. Vonder Haar, Observations of the global characteristics and regional radiative effects of marine cloud liquid water, *J. Clim.*, *8*, 2928–2946, 1995.

Gregory, G. L., et al., Air chemistry over the tropical forest of Guyana, *J. Geophys. Res.*, *91*, 8603–8612, 1986.

Grenfell, T. C., S. G. Warren, and P. C. Mullen, Reflection of solar radiation by the Antarctic snow surface at ultraviolet, visible, and near-infrared wavelengths, *J. Geophys. Res.*, *99*, 18,669–18,684, 1994.

Hack, J. J., J. T. Kiehl, and J. W. Hurrell, The hydrologic and thermodynamic characteristics of the NCAR CCM3, *J. Clim.*, *11*, 1179–1206, 1998.

Hamill, P., R. P. Turco, C. S. Kiang, O. B. Toon, and R. C. Whitten, An analysis of various nucleation mechanisms for sulfate particles in the stratosphere, *J. Aerosol. Sci.*, *13*, 561–585, 1982.

Hansen, J. E., and M. Sato, Trends of major climate forcing agents, *Proc. Natl. Acad. Sci.*, *93*, 14,778–14,783, 2001.

Hansen, A. D. A., B. A. Bodhaine, E. G. Dutton, and R. C. Schnell, Aerosol black carbon measurement at the South Pole: Initial results, 1986–1987, *Geophys. Res. Lett.*, *15*, 1193–1196, 1988.

Hansen, A. D. A., V. N. Kapustin, V. M. Kopeikin, D. A. Gillette, and B. A. Bodhaine, Optical absorption by aerosol black carbon and dust in a desert region of central Asia, *Atmos. Environ.*, *27A*, 25,227–25,331, 1993.

Hansen, J., M. Sato, and R. Ruedy, Radiative forcing and climate response, *J. Geophys. Res.*, *102*, 6831–6864, 1997.

Hansen, J., M. Sato, R. Ruedy, A. Lacis, and V. Oinas, Global warming in the twenty-first century: An alternative scenario, *Proc. Natl. Acad. Sci.*, *97*, 9875–9880, 2000.

Hayhoe, K., A. Jain, H. Pitcher, C. MacCracken, M. Gibbs, D. Wuebbles, R. Harvey, and D. Kruger, Costs of multigreenhouse gas reduction targets for the USA, *Science*, *286*, 905–906, 1999.

Haywood, J. M., D. L. Roberts, A. Slingo, J. M. Edwards, and K. P. Shine, General circulation model calculations of the direct radiative forcing by anthropogenic sulfate and fossil-fuel soot aerosol, *J. Clim.*, *10*, 1562–1577, 1997.

He, K., F. Yang, Y. Ma, Q. Zhang, X. Yao, C. K. Chan, S. Cadle, T. Chan, and P. Mulawa, The characteristics of PM2.5 in Beijing, China, *Atmos. Environ.*, *35*, 4959–4970, 2001.

Heidam, N. Z., P. Wahlin, and J. H. Christensen, Tropospheric gases and aerosols in Northeast Greenland, *J. Atmos. Sci.*, *56*, 261–278, 1998.

Heintzenberg, J., Size-segregated measurements of particulate elemental carbon and aerosol light absorption at remote Arctic locations, *Atmos. Environ.*, *16*, 2461–2469, 1982.

Heintzenberg, J., and A. Mészáros, Elemental carbon, sulfur, and metals in aerosol samples at a Hungarian regional air pollution station, *Időjárás*, *89*, 313–319, 1985.

Hillamo, R., V.-M. Kerminen, M. Aurela, T. Makela, W. Maenhaut, and C. Leck, Modal structure of chemical mass size distribution in the high Arctic aerosol, *J. Geophys. Res.*, *106*, 27,555–27,571, 2001.

Hitzenberger, R., and S. Tohno, Comparison of black carbon (BC) aerosols in two urban areas: Concentrations and size distributions, *Atmos. Environ.*, *35*, 2153–2167, 2001.

Hjellbrekke, A.-G. and J. E. Hanssen, Data report, 1996, 1, Annual summaries, *EMEP/CCC Rep. 1/98*, 85 pp., Norw. Inst. for Air Res., Lillestrom, 1998.

Hoffert, M. I., A. J. Callegari, and C. T. Hsieh, The role of deep sea heat storage in the secular response of climate forcing, *J. Geophys. Res.*, *85*, 6667–6679, 1980.

Im, J. S., V. K. Saxena, and B. N. Wenny, Temporal trends of black carbon concentrations and regional climate forcing in the southeastern United States, *Atmos. Environ.*, *35*, 3293–3302, 2001.

Intergovernmental Panel on Climate Change (IPCC), *Third Assessment Report, Climate Change 2001: The Scientific Basis*, edited by J. T. Houghton et al., Cambridge Univ. Press, New York, 2001.

International Energy Agency, *Oil Information 1998*, OECD/IED, Paris, 1999.

Jacobson, M. Z., *Developing, coupling, and applying a gas, aerosol, transport, and radiation model to study urban and regional air pollution*, Ph.D. Thesis, 436 pp., Univ. of Calif., Los Angeles, 1994.

Jacobson, M. Z., Development and application of a new air pollution modeling system, part II, Aerosol module structure and design, *Atmos. Environ.*, *31A*, 131–144, 1997a.

Jacobson, M. Z., Development and application of a new air pollution modeling system, part III, Aerosol-phase simulations, *Atmos. Environ.*, *31A*, 587–608, 1997b.

Jacobson, M. Z., Numerical techniques to solve condensational and dissolutional growth equations when growth is coupled to reversible reactions, *Aerosol Sci. Technol.*, *27*, 491–498, 1997c.

Jacobson, M. Z., Improvement of SMVGEAR II on vector and scalar machines through absolute error tolerance control, *Atmos. Environ.*, *32*, 791–796, 1998a.

Jacobson, M. Z., Studying the effects of aerosols on vertical photolysis rate coefficient and temperature profiles over an urban airshed, *J. Geophys. Res.*, *103*, 10,593–10,604, 1998b.

Jacobson, M. Z., *Fundamentals of Atmospheric Modeling*, 656 pp., Cambridge Univ. Press, New York, 1999a.

Jacobson, M. Z., Studying the effects of calcium and magnesium on size-distributed nitrate and ammonium with EQUISOLV II, *Atmos. Environ.*, *33*, 3635–3649, 1999b.

Jacobson, M. Z., Isolating nitrated and aromatic aerosols and nitrated aromatic gases as sources of ultraviolet light absorption, *J. Geophys. Res.*, *104*, 3527–3542, 1999c.

Jacobson, M. Z., A physically-based treatment of elemental carbon optics: Implications for global direct forcing of aerosols, *Geophys. Res. Lett.*, *27*, 217–220, 2000.

Jacobson, M. Z., Strong radiative heating due to the mixing state of black carbon in atmospheric aerosols, *Nature*, *409*, 695–697, 2001a.

Jacobson, M. Z., Global direct radiative forcing due to multicomponent anthropogenic and natural aerosols, *J. Geophys. Res.*, *106*, 1551–1568, 2001b.

Jacobson, M. Z., GATOR-GCMM: A global through urban scale air pollution and weather forecast model, 1, Model design and treatment of subgrid soil, vegetation, roads, rooftops, water, sea ice, and snow, *J. Geophys. Res.*, *106*, 5385–5402, 2001c.

Jacobson, M. Z., GATOR-GCMM, 2, A study of day- and nighttime ozone layers aloft, ozone in national parks, and weather during the SARMAP Field Campaign, *J. Geophys. Res.*, *106*, 5403–5420, 2001d.

Jacobson, M. Z., R. P. Turco, E. J. Jensen, and O. B. Toon, Modeling

coagulation among particles of different composition and size, *Atmos. Environ.*, *28*, 1327–1338, 1994.

Janssen, N. A. H., D. F. M. Van Mansom, K. Van der Jagt, H. Harssema, and G. Hoek, Mass concentration and elemental composition of airborne particulate matter at street and background locations, *Atmos. Environ.*, *31*, 1185–1193, 1997.

Johansen, A. M., R. L. Siefert, and M. R. Hoffmann, Chemical composition of aerosols collected over the tropical North Atlantic Ocean, *J. Geophys. Res.*, *105*, 15,277–15,312, 2000.

Jones, P. D., D. E. Parker, T. J. Osborn, and K. R. Briffa, Global and hemispheric temperature anomalies: Land and marine instrumental records, in *Trends Online: A Compendium of Data on Global Change*, Carbon Dioxide Inf. Anal. Cent., Oak Ridge Natl. Lab., U.S. Dept. of Energy, Oak Ridge, Tenn., USA, 1999.

Kadowaki, S., Characterization of carbonaceous aerosols in the Nagoya urban area, 1, Elemental and organic carbon concentrations and the origin of organic aerosols, *Environ. Sci. Technol.*, *24*, 741–744, 1990.

Kaneyasu, N., and S. Murayama, High concentrations of black carbon over middle latitudes in the North Pacific Ocean, *J. Geophys. Res.*, *105*, 19,881–19,890, 2000.

Keeler, G. J., S. M. Japar, W. W. Brachaczek, R. A. Gorse, J. M. Norbeck, and W. R. Pierson, The sources of aerosol elemental carbon at Allegheny Mountain, *Atmos. Environ.*, *24A*, 2795–2805, 1990.

Kerminen, V-M., K. Teinila, and R. Hillamo, Chemistry of sea-salt particles in the summer Antarctic atmosphere, *Atmos. Environ.*, *34*, 2817–2825, 2000.

Kettle, A. J., et al., A global database of sea surface dimethylsulfide (DMS) measurements and a procedure to predict sea surface DMS as a function of latitude, longitude, and month, *Global Biogeochem. Cycles*, *13*, 399–444, 1999.

Kim, B. M., S. Teffera, and M. D. Zeldin, Characterization of PM2.5 and PM10 in the South Coast Air Basin of Southern California, part 1, Spatial variations, *J. Air Waste Manage. Assoc.*, *50*, 2034–2044, 2000.

Klein, S., Synoptic variability of low-cloud properties and meteorological parameters in the subtropical trade wind boundary layer, *J. Clim.*, *10*, 2018–2039, 1997.

Knutson, T. R., T. L. Delworth, K. W. Dixon, and R. J. Stouffer, Model assessment of regional surface temperature trends (1949–1997), *J. Geophys. Res.*, *104*, 30,981–30,996, 1999.

Kopeyken, V. M., V. N. Kapustin, and M. S. Pekur, Monitoring of soot aerosol in the atmosphere of Moscow, *Izv. Acad. Sci. USSR, Atmos. Ocean. Phys. Engl. Transl.*, *29*, 198–202, 1993.

Krekov, G. M., Models of atmospheric aerosols, in *Aerosol Effects on Climate*, edited by S. G. Jennings, pp. 9–72, Univ. of Ariz. Press, Tucson, 1993.

Krivacsy, Z., A. Hoffer, Zs. Sarvari, D. Temesi, U. Baltensperger, S. Nyeki, E. Weingartner, S. Kleefeld, and S. G. Jennings, Role of organic and black carbon in the chemical composition of atmospheric aerosol at European background sites, *Atmos. Environ.*, *35*, 6231–6244, 2001.

Light, B., H. Eicken, G. A. Maykut, and T. C. Grenfell, The effect of included particulates on the spectral albedo of sea ice, *J. Geophys. Res.*, *103*, 27,739–27,752, 1998.

Lighty, J. A., J. M. Veranth, and A. F. Sarofim, Combustion aerosols: Factors governing their size and composition and implications to human health, *J. Air Waste Manage. Assoc.*, *50*, 1565–1618, 2000.

Lin, J. J., and H.-S. Tai, Concentrations and distributions of carbonaceous species in ambient particles in Kaohsiung City, Taiwan, *Atmos. Environ.*, *35*, 2627–2636, 2001.

Liss, P. S., and L. Merlivat, Air–sea gas exchange rates, in *The Role of Air–Sea Exchange in Geochemical Cycling*, edited by P. Buat-Menard, pp. 113–127, 1986.

Lobert, J. M., W. C. Keene, J. A. Logan, and R. Yevich, Global chlorine emissions from biomass burning: Reactive chlorine emissions inventory, *J. Geophys. Res.*, *104*, 8373–8389, 1999.

Lu, R., and R. P. Turco, Air pollutant transport in a coastal environment, part I, Two-dimensional simulations of sea-breeze and mountain effects, *J. Atmos. Sci.*, *51*, 2285–2308, 1994.

Lyubovtseva, Y. S., and L. G. Yatskovich, Soot in the aerosols of different regions, *J. Aerosol Sci.*, *20*, 1269–1272, 1989.

Maricq, M. M., R. E. Chase, D. H. Podsiadlik, and R. Vogt, Vehicle exhaust particle size distributions: A comparison of tailpipe and dilution tunnel measurements, *SAE Technical Paper 1999-01-1461, SAE*, 1999a.

Maricq, M. M., D. H. Posiadlik, and R. C. Chase, Examination of the size-resolved and transient nature of motor vehicle particle emissions, *Environ. Sci. Technol.*, *33*, 1618–1626, 1999b.

Marland, G., T. A. Boden, R. J. Andres, A. L. Brenkert, and C. Johnston, Global, regional, and national CO_2 emissions, in *Trends Online: A Compendium of Data on Global Change*, Carbon Dioxide Inf. Anal. Cent., Oak Ridge Natl. Lab., U.S. Dept. of Energy, Oak Ridge, Tenn., USA, 1999.

Marticorena, B., G. Bergametti, B. Aumont, Y. Callot, and M. Legrand, Modeling the atmospheric dust cycle, 2, Simulation of Saharan dust sources, *J. Geophys. Res.*, *102*, 4387–4404, 1997.

McNaughton, D. J., and R. J. Vet, Eulerian model evaluation field study (EMEFS): A summary of surface network measurements and data quality, *Atmos. Environ.*, *30*, 227–238, 1996.

Mellor, G. L., and T. Yamada, Development of a turbulence closure model for geophysical fluid problems, *Rev. Geophys. Space Phys.*, *20*, 851–875, 1982.

Mlawer, E. J., S. J. Taubman, P. D. Brown, M. J. Iacono, and S. A. Clough, Radiative transfer for inhomogeneous atmospheres: RRTM, a validated correlated-*k* model for the longwave, *J. Geophys. Res.*, *102*, 16,663–16,682, 1997.

Modey, W. K., Y. Pang, N. L. Eatough, and D. J. Eatough, Fine particulate (PM2.5) composition in Atlanta, USA: Assessment of the particle concentrator-Brigham Young University organic sampling system, PC-BOSS, during the EPA supersite study, *Atmos. Environ.*, *35*, 6493–6502, 2001.

Monahan, E. C., D. E. Spiel, and K. L. Davidson, A model of marine aerosol generation via whitecaps and wave disruption in oceanic whitecaps, in *Oceanic whitecaps and their role in air–sea exchange processes*, edited by E. C. Monahan and G. M. Niocaill, pp. 167–174, D. Reidel, Norwell, Mass., 1986.

Mukai, H., Y. Ambe, K. Shibata, T. Muku, K. Takeshita, T. Fukuma, J. Takahashi, and S. Mizota, Long term variation of chemical composition of atmospheric aerosol on the Oki Islands in the Sea of Japan, *Atmos. Environ.*, *24A*, 1379–1390, 1990.

Nicholls, S., The dynamics of stratocumulus: Aircraft observations and comparisons with a mixed layer model, *Q. J. R. Meteorol. Soc.*, *110*, 783–820, 1984.

Nijssen, B., R. Schnur, and D. P. Lettenmaier, Global retrospective estimation of soil moisture using the variable infiltration capacity land surface model, 1980–1993, *J. Clim.*, *14*, 1790–1808, 2001.

Noone, K. J., and A. D. Clarke, Soot scavenging measurements in Arctic snowfall, *Atmos. Environ.*, *22*, 2773–2778, 1988.

O'Dowd, C. D., M. H. Smith, and S. G. Jennings, Submicron particle, radon, and soot carbon characteristics over the northeast Atlantic, *J. Geophys. Res.*, *98*, 1123–1135, 1993.

Offenberg, J. H., and J. E. Baker, Aerosol size distributions of elemental and organic carbon in urban and over-water atmospheres, *Atmos. Environ.*, *34*, 1509–1517, 2000.

Ohta, S., and T. Okita, Measurements of particulate carbon from the atmosphere, *Sci. Total Environ.*, *18*, 2439–2445, 1984.

Olivier, J. G. J., A. F. Bouwman, C. W. M. Van der Maas, J. J. M. Berdowski, C. Veldt, J. P. J. Bloos, A. J. H. Visschedijk, P. Y. J. Zandveld, and J. L. Haverlag, Description of EDGAR Version 2.0: A set of global emission inventories of greenhouse gases and ozone-depleting substances for all anthropogenic and most natural sources on a per country basis on $1° \times 1°$ grid, *National Institute of Public Health and the Environment, RIVM report no. 771060 002/TNO-MEP report no. R96/119*, 1996.

Oltmans, S. J., and D. J. Hofmann, Increase in lower-stratospheric water vapour at a mid-latitude Northern Hemisphere site from 1981–1994, *Nature*, *374*, 146–149, 1995.

Park, S. S., Y. J. Kim, and K. Fung, Characteristics of PM2.5 carbonaceous aerosol in the Sihwa industrial area, South Korea, *Atmos. Environ.*, *35*, 657–665, 2001.

Parungo, F., C. Nagamoto, M-Y. Zhou, D. A. Hansen, and J. Harris, Aeolian transport of aerosol black carbon from China to the ocean, *Atmos. Environ.*, *28*, 3251–3260, 1994.

Polissar, A. V., Measurements of the soot mass concentration and particle-size distribution of atmospheric aerosol in the eastern Arctic, *Izv. Acad. Sci. USSR, Atmos. Ocean. Phys. Engl. Transl.*, *29*, 66–73, 1993.

Pope, C. A., III and D. W. Dockery, Epidemiology of particle effects, in *Air Pollution and Health*, edited by S. T. Holgate et al., pp. 673–705, Academic, San Diego, Calif., 1999.

Pruppacher, H. R., and J. D. Klett, *Microphysics of Clouds and Precipitation*, 2nd rev. and enl. ed., Kluwer Acad., Norwell, Mass., 1997.

Puxbaum, H., J. Rendl, R. Allabashi, L. Otter, and M. C. Scholes, Mass balance of the atmospheric aerosol in a South African subtropical savanna (Nylsvley, May 1997), *J. Geophys. Res.*, *105*, 20,697–20,706, 2000.

Quinn, P. K., D. J. Coffman, T. S. Bates, T. L. Miller, J. E. Johnson, K. Voss, E. J. Welton, and C. Neusus, Dominant aerosol chemical components and their contribution to extinction during the Aerosols99 cruise across the Atlantic, *J. Geophys. Res.*, *106*, 20,783–20,809, 2001.

Raunemaa, T., K. Kuuspalo, T. Alander, E. Tamm, A. Mirme, and V. Laine, Black carbon and aerosol in Böisto Island, *J. Aerosol Sci.*, *24*, S29–S30, 1993.

Reid, J. S., and P. V. Hobbs, Physical and optical properties of young smoke from individual biomass fires in Brazil, *J. Geophys. Res.*, *103*, 32,013–32,030, 1998.

Ruellan, S., and H. Cachier, Characterization of fresh particulate vehicular exhausts near a Paris high flow road, *Atmos. Environ.*, *35*, 453–468, 2001.
Savoie, D. L., J. M. Prospero, R. J. Larsen, F. Huang, M. Izaguirre, T. Huang, T. H. Snowdon, L. Custals, and C. G. Sanderson, Nitrogen and sulfur species in Antarctic aerosols at Mawson, Palmer Station, and March (King George Island), *J. Atmos. Chem.*, *17*, 95–122, 1993.
Savoie, D. L., J. M. Prospero, R. Arimoto, and R. A. Duce, Non-sea-salt sulfate and methanesulfonate at American Samoa, *J. Geophys. Res.*, *99*, 3587–3596, 1994.
Schneider, T., and I. M. Held, Discriminants of twentieth-century changes in earth surface temperatures, *J. Clim.*, *14*, 249–254, 2001.
Shauer, J. J., M. J. Kleeman, G. R. Cass, and B. R. T. Simoneit, Measurement of emissions from air pollution sources, 2, C_1 through C_{30} compounds from medium duty trucks, *Environ. Sci. Technol.*, *33*, 1578–1587, 1999.
Smith, S. J., T. M. L. Wigley, and J. Edmonds, A new route toward limiting climate change, *Science*, *290*, 1109–1110, 2000.
Spadaro, J. V., and A. Rabl, Damage costs due to automotive air pollution and the influence of street canyons, *Atmos. Environ.*, *35*, 4763–4775, 2001.
Stelson, A. W., Urban aerosol refractive index prediction by partial molar refraction approach, *Environ. Sci. Technol.*, *24*, 1676–1679, 1990.
Stern, D. I., and R. K. Kaufman, Annual estimates of global anthropogenic methane emissions: 1860–1994, in *Trends Online: A Compendium of Data on Global Change*, Carbon Dioxide Inf. Anal. Cent., Oak Ridge Natl. Lab., U.S. Dept. of Energy, Oak Ridge, Tenn., USA, 1998.
Strader, R., F. Lurmann, and S. N. Pandis, Evaluation of secondary organic aerosol formation in winter, *Atmos. Environ.*, *33*, 4849–4863, 1999.
Streets, D. G., S. Gupta, S. T. Waldhoff, M. Q. Wang, T. C. Bond, and B. Yiyun, Black carbon emissions in China, *Atmos. Environ.*, *35*, 4281–4296, 2001.
Stott, P. A., S. F. B. Tett, G. S. Jones, M. R. Allen, J. F. B. Mitchell, and G. J. Jenkins, External control of 20th century temperature by natural and anthropogenic forcings, *Science*, *290*, 2133–2137, 2000.
Talbot, R. W., M. O. Andreae, H. Berresheim, P. Artaxo, M. Garstang, R. C. Harriss, K. M. Beecher, and S. M. Li, Aerosol chemistry during the wet season in central Amazonia: The influence of long-range transport, *J. Geophys. Res.*, *95*, 16,955–16,969, 1990.
Tang, I., Thermodynamic and optical properties of mixed-salt aerosols of atmospheric importance, *J. Geophys. Res.*, *102*, 1883–1893, 1997.
Temesi, D., A. Molnar, E. Meszaros, T. Feczko, A. Gelencser, G. Kiss, and Z. Krivacsy, Size resolved chemical mass balance of aerosol particles over rural Hungary, *Atmos. Environ.*, *35*, 4347–4355, 2001.
Toon, O. B., and T. P. Ackerman, Algorithms for the calculation of scattering by stratified spheres, *Appl. Opt.*, *20*, 3657–3660, 1981.
Toon, O. B., C. P. McKay, T. P. Ackerman, and K. Santhanam, Rapid calculation of radiative heating rates and photodissociation rates in inhomogeneous multiple scattering atmospheres, *J. Geophys. Res.*, *94*, 16,287–16,301, 1989.
Twomey, S. A., The effect of cloud scattering on the absorption of solar radiation by atmospheric dust, *J. Atmos. Sci.*, *29*, 1156–1159, 1977.
United States Geological Survey (USGS), U. Nebraska, Lincoln/European Commission's Joint Research Center 1-km resolution global landcover characteristics data base, derived from Advanced Very High Resolution Radiometer (AVHRR) data from the period April 1992 to March 1993, 1999.
Venkatram, A., and R. Viskanta, Radiative effects of elevated pollutant layers, *J. Appl. Meteorol.*, *16*, 1256–1272, 1977.
Vogelmann, A. M., A. Robock, and R. G. Ellingson, Effects of dirty snow in nuclear winter simulations, *J. Geophys. Res.*, *93*, 5319–5332, 1988.
Voldner, E. C., Y.-F. Li, M. T. Scholtz, and K. A. Davidson, $1^\circ \times 1^\circ$ global SO_x and NO_x 2-level inventory resolved seasonally into emission sectors and point and area emissions sources, Global Emissions Inventory Activity (GEIA) website www.onesky.umich.edu/geia/, 1999.
Walcek, C. J., and N. M. Aleksic, A simple but accurate mass conservative, peak-preserving, mixing ratio bounded advection algorithm with FORTRAN code, *Atmos. Environ.*, *32*, 3863–3880, 1998.
Walmsley, J. L., and M. L. Wesely, Modification of coded parameterizations of surface resistances to gaseous dry deposition, *Atmos. Environ.*, *30A*, 1181–1188, 1996.
Wang, M. Q., GREET 1.5: Transportation fuel-cycle model, volume 1, Methodology, development, use, and results, *Argonne Natl. Lab. Rep. No. ANL/ESD-39*, Vol. 1, 1999.
Wang, C., and R. G. Prinn, On the roles of deep convective clouds in tropospheric chemistry, *J. Geophys. Res.*, *105*, 22,269–22,297, 2000.
Warren, S. G., Impurities in snow: Effects on albedo and snowmelt, *Ann. Glaciol.*, *5*, 177–179, 1984.
Warren, S. G., and A. D. Clarke, Soot in the atmosphere and snow surface of Antarctica, *J. Geophys. Res.*, *95*, 1811–1816, 1990.
Wesely, M. L., Parameterization of surface resistances to gaseous dry deposition in regional-scale numerical models, *Atmos. Environ.*, *23*, 1293–1304, 1989.
Willison, M. J., A. G. Clarke, and E. M. Zeki, Seasonal variation in atmospheric aerosol concentration and composition at urban and rural sites in northern England, *Atmos. Environ.*, *19*, 1081–1089, 1985.
Wolff, G. T., M. S. Ruthkosky, D. P. Stroup, P. E. Korsog, M. A. Ferman, G. J. Wendel, and D. H. Stedman, Measurements of SOx, NOx and aerosol species on Bermuda, *Atmos. Environ.*, *20*, 1229–1239, 1986.
World Health Organization (WHO), http://www.who, 2000.
Wu, J., on of spume drops by the wind tearing of wave crests: The search for quantification, *J. Geophys. Res.*, *98*, 18,221–18,227, 1993.
Xie, P., and P. A. Arkin, Analyses of global monthly precipitation using gauge observations, satellite estimates, and numerical model predictions, *J. Clim.*, *9*, 840–858, 1996.
Zappoli, S., et al., Inorganic, organic and macromolecular components of fine aerosol in different areas of Europe in relation to their water solubility, *Atmos. Environ.*, *33*, 2733–2743, 1999.
Zdunkowski, W. G., R. M. Welch, and J. Paegle, One dimensional numerical simulation of the effects of air pollution on the planetary boundary layer, *J. Atmos. Sci.*, *33*, 2399–2414, 1976.
Zeng, X., R. E. Dickinson, A. Walker, M. Shaikh, R. S. DeFries, and J. Qi, Derivation and evaluation of global 1-km fractional vegetation cover data for land modeling, *J. Appl. Meteorol.*, *39*, 826–839, 2000.
Zhao, J., and R. P. Turco, Nucleation simulations in the wake of a jet aircraft in stratospheric flight, *J. Aerosol Sci.*, *26*, 779–795, 1995.
Zier, M., Mass concentrations of total dust and soot in the near surface air in east Germany, *J. Aerosol Sci.*, *22*, S597–S600, 1991.

M. Z. Jacobson, Department of Civil and Environmental Engineering, Stanford University, Terman Engineering Center, Room M-13, Stanford, CA 94305-4020, USA. (jacobson@ce.stanford.edu)